A CELL-CENTERED LAGRANGIAN SCHEME FOR TWO-DIMENSIONAL COMPRESSIBLE FLOW PROBLEMS*

PIERRE-HENRI MAIRE†, RÉMI ABGRALL‡, JÉRÔME BREIL†, AND JEAN OVADIA§

Abstract. We present a new Lagrangian cell-centered scheme for two-dimensional compressible flows. The primary variables in this new scheme are cell-centered, i.e., density, momentum, and total energy are defined by their mean values in the cells. The vertex velocities and the numerical fluxes through the cell interfaces are not computed independently, contrary to standard approaches, but are evaluated in a consistent manner due to an original solver located at the nodes. The main new feature of the algorithm is the introduction of four pressures on each edge, two for each node on each side of the edge. This extra degree of freedom allows us to construct a nodal solver which fulfills two properties. First, the conservation of momentum and total energy is ensured. Second, a semidiscrete entropy inequality is provided. In the case of a one-dimensional flow, the solver reduces to the classical Godunov acoustic solver: it can be considered as its two-dimensional generalization. Many numerical tests are presented. They are representative test cases for compressible flows and demonstrate the robustness and the accuracy of this new solver.

Key words. Godunov-type schemes, hyperbolic conservation laws, Lagrangian gas dynamics

AMS subject classifications. 65M06, 76L05, 76N05

DOI. 10.1137/050633019

1. Introduction. The physical model that is considered throughout this paper is based on the equations of fluid dynamics written in Lagrangian form. This form is well adapted to the simulation of multimaterial compressible fluid flows, such as those encountered in the domain of inertial confinement fusion (ICF); see [19] and [25]. Our aim is to propose a new Lagrangian cell-centered scheme for two-dimensional gas dynamics equations. Before describing our method, let us briefly give a historical overview of the Lagrangian schemes.

Lagrangian schemes are characterized by a mesh that follows the fluid flow. In this way, these methods treat interfaces in a natural manner. The main numerical difficulty lies in the node motion discretization, especially for multidimensional situations. The most natural way to overcome this difficulty is to use a staggered discretization, where the momentum is defined at the nodes and the other variables (density, pressure, and specific internal energy) are cell-centered. This type of scheme was first introduced by von Neumann and Richtmyer in [27] for one-dimensional flows. The bidimensional extension was proposed by Wilkins in [29]. It is based on an internal energy formulation. The entropy production inherent to shock waves is ensured by an artificial viscosity. In its initial version, this scheme was not conservative, and it admitted numerical spurious modes. However, in spite of these drawbacks, this scheme has been widely used in the domain of multimaterial flow simulations during the last forty years. Moreover, in the past decade, many improvements have been made in order to solve the previous problems. In their paper [7], Caramana and Shashkov show

that with an appropriate discretization of the subzonal forces resulting from subzonal pressures, hourglass motion and spurious vorticity can be eliminated. By using the method of support operators proposed in [6], they constructed a staggered scheme which ensures the conservation of total energy. Moreover, the discretization of artificial viscosity has been considerably improved: first, by introducing formulations for multidimensional shock wave computations in [5] and then by using a discretization based on a mimetic finite difference scheme in [4]. With all these improvements, the staggered Lagrangian scheme is an accurate and robust method, which can produce impressive results, even on unstructured polygonal grids; see, for instance, [21].

An alternative to the staggered discretization is to use a conservative cell-centered discretization. This method for Lagrangian gas dynamics in one dimension was introduced by Godunov; see [12] and [24]. The multidimensional extension of this method was performed during the 1980s [2], [11]. This multidimensional scheme is a cell-centered finite volume scheme on moving structured or unstructured meshes. It is constructed by integrating directly the system of conservation laws on each moving cell. The primary variables—density, momentum, and total energy—are defined in the cells. The flux across the boundary of the cell is computed by solving exactly or approximately a one-dimensional Riemann problem in the direction normal to the boundary. The main problem with this type of method lies in the fact that the node velocity needed to move the mesh cannot be directly calculated. In [2], the node velocity is computed via a special least squares procedure. It consists in minimizing the error between the normal velocity coming from the Riemann solver and the normal projection of the vertex velocity. It turns out that it leads to an artificial grid motion, which requires a very expensive treatment [10]. Moreover, with this approach the flux calculation is not consistent with the node motion.

Recently, new cell-centered methods have been proposed in [15] and [1]. These new approaches use a fully Lagrangian form of the gas dynamics equations; that is, the gradient and divergence operators are expressed in the Lagrangian coordinates. This type of discretization needs to compute the Jacobian matrix associated to the map between Lagrangian and Eulerian spaces. However, these methods are purely Lagrangian and cannot be interpreted as moving mesh methods. This drawback has motivated another approach proposed by Després and Mazeran. In [9], they made a theoretical analysis of the Lagrangian gas dynamics equations written in a fully Lagrangian form and they derived a new conservative and entropy consistent two-dimensional Lagrangian scheme of the finite volume type. It is a moving grid scheme based on a nodal solver. The node velocity is computed in a coherent manner with the face fluxes. The numerical results shown in [9] are quite impressive, in particular, those related to the difficult Saltzmann's test case. However, it appears that in the case of one-dimensional flows, this scheme leads to a nodal velocity, which depends on the cell aspect ratio. This drawback has motivated our study to develop a new cell-centered scheme that retains the good feature of the Després–Mazeran scheme but resolves the aspect ratio problem. Here, we propose a new Lagrangian cell-centered scheme in which the vertex velocities and the numerical fluxes through the cell interfaces are not computed independently as usual but in a consistent manner with an original solver located at the nodes. The main new feature of the algorithm is the introduction of four pressures on each edge, two for each node on each side of the edge. This is the main difference from [9]. We show, in the limit of a one-dimensional flow computed by our two-dimensional solver, or for flows in a cylindrical geometry, that the scheme recovers the classical Godunov approximate Riemann solver. Moreover, our scheme locally conserves momentum and total energy and satisfies a local entropy inequality.

The boundary conditions are taken into account in a natural way. This scheme is first order in time and space.

The paper is organized as follows. First we recall the gas dynamics equations written in the Lagrangian form. In section 2 we derive space approximations based on face and node fluxes. Then we build a nodal solver using conservation arguments and a discrete entropy inequality. In section 4 we give the time discretization. Finally, we validate our new scheme with several test cases. They are representative test cases for compressible fluid flows and demonstrate the robustness and the accuracy of this new solver.

2. Derivation of the Euler equations in the Lagrangian formalism. The aim of this section is to recall briefly how the gas dynamics equations are obtained in the Lagrangian formalism. For such a derivation, we follow the approach developed in [8].

Let $\mathcal{D}$ be a region of the two-dimensional space $\mathbb{R}^2$, filled with an inviscid fluid and equipped with an orthonormal frame (O, X, Y). The Lagrangian formalism consists in following the time evolution of fluid particles along their trajectories. Consider a fluid particle which is moving through the point M at time $t > 0$ and whose initial position is point m. The coordinates of point M are denoted by (X, Y) and are named Eulerian coordinates. The coordinates of point m are denoted by (x, y) and are named Lagrangian coordinates. The Eulerian coordinates are obtained from the trajectory equations

$$(2.1) \qquad \begin{aligned} \frac{dX}{dt} &= u(X, Y, t), \quad X(x, y, 0) = x, \\[6pt] \frac{dY}{dt} &= v(X, Y, t), \quad Y(x, y, 0) = y, \end{aligned}$$

where (u, v) are the coordinates of the fluid velocity $\boldsymbol{V}$. If the velocity field is smooth enough, the system (2.1) admits a unique solution $(X(x, y, t), Y(x, y, t))$. This enables us to define the map

$$(2.2) \qquad \mathcal{M}_t : (x, y) \mapsto (X, Y),$$

where (X, Y) is the unique solution of (2.1). With fixed t, this map advances each fluid particle from its position at time $t = 0$ to its position at time t. If ω denotes a region in $\mathcal{D}$, then $\mathcal{M}_t(\omega) = \Omega$ is the volume ω moving with the fluid. We assume that for each $t > 0$, $\mathcal{M}_t$ is invertible. Let us introduce the Jacobian of this map:

$$(2.3) \qquad J(x, y, t) = \begin{vmatrix} \dfrac{\partial X}{\partial x} & \dfrac{\partial X}{\partial y} \\[10pt] \dfrac{\partial Y}{\partial x} & \dfrac{\partial Y}{\partial y} \end{vmatrix}.$$

We notice that $J(x, y, 0) = 1$ and since $\mathcal{M}_t$ is invertible we have for each $t > 0$, $J(x, y, t) > 0$. Time differentiation of (2.3) gives the classical result

$$(2.4) \qquad \frac{dJ}{dt} - J\nabla \cdot \boldsymbol{V} = 0,$$

where $\nabla\cdot$ denotes the divergence operator, namely, $\nabla \cdot \boldsymbol{V} = \frac{\partial u}{\partial X} + \frac{\partial v}{\partial Y}$.

Let us consider a flow variable φ depending on Eulerian coordinates: $\varphi \equiv \varphi(X, Y, t)$. Time differentiation of φ gives

$$\frac{d\varphi}{dt} = \frac{\partial \varphi}{\partial t} + \frac{dX}{dt}\frac{\partial \varphi}{\partial X} + \frac{dY}{dt}\frac{\partial \varphi}{\partial Y},$$

and using (2.1) one obtains

$$(2.5) \qquad \frac{d\varphi}{dt} = \frac{\partial \varphi}{\partial t} + \boldsymbol{\nabla}\varphi \cdot \boldsymbol{V},$$

where $\boldsymbol{\nabla}$ is the gradient operator, namely $\boldsymbol{\nabla}\varphi = (\frac{\partial \varphi}{\partial X}, \frac{\partial \varphi}{\partial Y})^t$. The time derivative of φ depending on Eulerian coordinates is named the material derivative; it represents the variation of φ along a fluid trajectory. Finally, combining (2.4) and (2.5) it is straightforward to write

$$(2.6) \qquad \frac{d}{dt}(\varphi J) = J\left[\frac{\partial \varphi}{\partial t} + \nabla \cdot (\varphi \boldsymbol{V})\right].$$

With this last equation we are able to transform gas dynamics equations written in Eulerian formalism. These equations for an inviscid compressible fluid (see [18]) are

$$\frac{\partial \rho}{\partial t} + \nabla \cdot (\rho \boldsymbol{V}) = 0,$$

$$(2.7) \qquad \frac{\partial}{\partial t}(\rho \boldsymbol{V}) + \boldsymbol{\nabla} \cdot (\rho \boldsymbol{V} \otimes \boldsymbol{V}) + \boldsymbol{\nabla}P = \boldsymbol{0},$$

$$\frac{\partial}{\partial t}(\rho E) + \nabla \cdot (\rho E \boldsymbol{V}) + \nabla \cdot (P \boldsymbol{V}) = 0.$$

In (2.7), ρ denotes the density, P is the pressure, and E is the specific total energy. We denote by $\varepsilon = E - \frac{1}{2}\|\boldsymbol{V}\|^2$ the specific internal energy. The thermodynamic closure of (2.7) is given by the equation of state, $P \equiv P(\rho, \varepsilon)$.

Now, using (2.6) for the conservative variables $\varphi = 1$, ρ, $\rho\boldsymbol{V}$, ρE and after substitution in (2.7), one obtains the gas dynamics system in Lagrangian formalism:

$$\frac{dJ}{dt} - J\nabla \cdot \boldsymbol{V} = 0,$$

$$\frac{d}{dt}(\rho J) = 0,$$

$$(2.8) \qquad \frac{d}{dt}(\rho J \boldsymbol{V}) + J\boldsymbol{\nabla}P = \boldsymbol{0},$$

$$\frac{d}{dt}(\rho J E) + J\nabla \cdot (P\boldsymbol{V}) = 0.$$

We notice that these equations are only in a semi-Lagrangian formalism since the gradient and divergence operate on variables which depend on Eulerian coordinates. In order to write these equations in a full Lagrangian way, one has to express the gradient and divergence operators with Lagrangian coordinates using the map $\mathcal{M}_t$. For such an approach, the reader should refer to [15], [20], and [9].

In order to perform the space discretization in the next section, we give the integral form of system (2.8). This form is obtained by integration of (2.8) on the Lagrangian domain ω. Knowing that $\mathcal{M}_t(\omega) = \Omega$ and $J\mathrm{d}\omega = \mathrm{d}\Omega$, using Green's formula one gets

$$(2.9\,\mathrm{i}) \qquad \frac{d}{dt}\int_\Omega \mathrm{d}\Omega - \int_{\partial\Omega} \boldsymbol{V}\cdot\boldsymbol{N}\,\mathrm{d}l = 0,$$

$$(2.9\,\mathrm{ii}) \qquad \frac{d}{dt}\int_\Omega \rho\,\mathrm{d}\Omega = 0,$$

$$(2.9\,\mathrm{iii}) \qquad \frac{d}{dt}\int_\Omega \rho\boldsymbol{V}\,\mathrm{d}\Omega + \int_{\partial\Omega} P\boldsymbol{N}\,\mathrm{d}l = \boldsymbol{0},$$

$$(2.9\,\mathrm{iv}) \qquad \frac{d}{dt}\int_\Omega \rho E\,\mathrm{d}\Omega + \int_{\partial\Omega} P\boldsymbol{V}\cdot\boldsymbol{N}\,\mathrm{d}l = 0,$$

where $\partial\Omega$ is the boundary of Ω, $\boldsymbol{N}$ is the unit outward normal to $\partial\Omega$, and $\mathrm{d}l$ is the length element on $\partial\Omega$. The equations (2.9 i)–(2.9 iv) are well known and have been used in this form in many papers; see, for example, [14]. Let m_Ω denote the mass of fluid enclosed in Ω. Then (2.9 ii) simply states mass conservation; hence for each time one gets $m_\Omega = m_\omega$. Let us introduce the area of domain Ω:

$$\mathcal{A}_\Omega = \int_\Omega \mathrm{d}\Omega.$$

We define the density $\rho_\Omega = \frac{m_\omega}{\mathcal{A}_\Omega}$ and the specific volume $\tau_\Omega = \frac{1}{\rho_\Omega}$. We also define the mass averaged velocity and total energy

$$\boldsymbol{V_\Omega} = \frac{1}{m_\omega}\int_\Omega \rho\boldsymbol{V}\mathrm{d}\Omega,$$

$$E_\Omega = \frac{1}{m_\omega}\int_\Omega \rho E\mathrm{d}\Omega.$$

With this notation and mass conservation, one gets the final integral form which will be useful for space discretization:

$$(2.10\,\mathrm{i}) \qquad m_\omega\frac{d}{dt}\tau_\Omega - \int_{\partial\Omega} \boldsymbol{V}\cdot\boldsymbol{N}\,\mathrm{d}l = 0,$$

$$(2.10\,\mathrm{ii}) \qquad m_\omega\frac{d}{dt}\boldsymbol{V_\Omega} + \int_{\partial\Omega} P\boldsymbol{N}\,\mathrm{d}l = \boldsymbol{0},$$

$$(2.10\,\mathrm{iii}) \qquad m_\omega\frac{d}{dt}E_\Omega + \int_{\partial\Omega} P\boldsymbol{V}\cdot\boldsymbol{N}\,\mathrm{d}l = 0,$$

where m_ω is the mass of fluid enclosed initially in ω.

3. Spatial approximation. Using classical finite volume approach, we derive in this section the spatial approximation of the gas dynamics equations written in Lagrangian formalism. Let us introduce some notation.
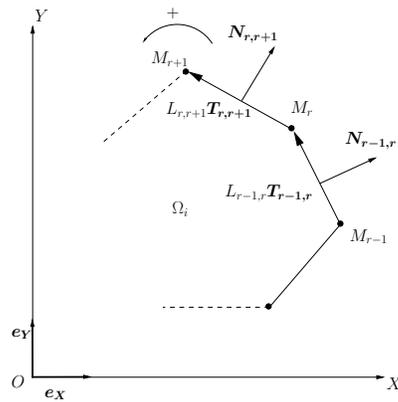
FIG. 3.1. *Notation.*

3.1. Notation, assumptions, and problem statement. Let $\{\omega_i,\ i = 1 \ldots I\}$ be a collection of nonoverlapping polygons whose reunion covers ω, the subdomain of $\mathbb{R}^2$ that is initially filled by the fluid. We set $\Omega_i = \mathcal{M}_t(\omega_i)$, where $\mathcal{M}_t$ is the map defined by (2.2). Ω_i is also a polygonal cell[1] whose vertices are denoted by $M_r,\ r = 1, \ldots, R(i)$. We denote by $R(i)$ the number of vertices (or faces) of the cell Ω_i. The vertices are indexed counterclockwise; see Figure 3.1. The numbering is also periodic; i.e., $M_{R(i)+1} = M_1$ and $M_0 = M_{R(i)}$. The frame (O, X, Y) is equipped with an orthonormal basis $(\boldsymbol{e_X}, \boldsymbol{e_Y})$ which is completed by the vector $\boldsymbol{e_Z} = \boldsymbol{e_X} \times \boldsymbol{e_Y}$. We denote the Eulerian coordinates of the vertex M_r by (X_r, Y_r). Note that M_r and its coordinates are time dependent. Considering any edge $[M_r, M_{r+1}]$ of Ω_i, $L_{r,r+1}$ denotes its length, $\boldsymbol{T_{r,r+1}}$ represents its unit tangent vector in a counterclockwise orientation, and $\boldsymbol{N_{r,r+1}}$ is its unit outward normal vector. Following these definitions and conventions, we have

$$
\begin{aligned}
L_{r,r+1}\boldsymbol{T_{r,r+1}} &= \boldsymbol{M_r M_{r+1}}, \\
L_{r,r+1}\boldsymbol{N_{r,r+1}} &= L_{r,r+1}\boldsymbol{T_{r,r+1}} \times \boldsymbol{e_Z}.
\end{aligned}
\tag{3.1}
$$

The fluid in cell Ω_i is described by the discrete variables $(\tau_i, \boldsymbol{V_i}, E_i)$, respectively, the averaged specific volume, velocity, and specific total energy. A set of discrete equations is written for these discrete unknowns, using the integral formulation (2.10 i) applied for cell Ω_i:

$$
m_i \frac{d}{dt}\tau_i - \int_{\partial \Omega_i} \boldsymbol{V} \cdot \boldsymbol{N}\, \mathrm{d}l = 0,
$$

$$
m_i \frac{d}{dt}\boldsymbol{V_i} + \int_{\partial \Omega_i} P\boldsymbol{N}\, \mathrm{d}l = \boldsymbol{0},
$$

$$
m_i \frac{d}{dt}E_i + \int_{\partial \Omega_i} P\boldsymbol{V} \cdot \boldsymbol{N}\, \mathrm{d}l = 0,
$$

---

[1] Here, we assume that Ω_i is still a polygon. This means that we implicitly assume that the velocity field variation is linear in space. This is not restrictive here, because the aim of the paper is to develop a scheme that is first order in space.

where m_i denotes the mass of the cell Ω_i. We also introduce the density $\rho_i = \frac{1}{\tau_i}$, the specific internal energy $\varepsilon_i = E_i - \frac{1}{2}\|\mathbf{V_i}\|^2$, and the pressure given by the equation of state $P_i = P(\rho_i, \varepsilon_i)$. Since all fluid variables are assumed to be constant in cell Ω_i, we obtain a spatial approximation which is first order accurate.

Finally, we introduce some notation to express the discrete face fluxes. Let us denote by $\mathbf{V^{\star}_{r,r+1}} \cdot \mathbf{N_{r,r+1}}$, $P^{\star}_{r,r+1}\mathbf{N_{r,r+1}}$, and $(P\mathbf{V})^{\star}_{r,r+1} \cdot \mathbf{N_{r,r+1}}$ the volume, momentum, and total energy fluxes on the face $[M_r, M_{r+1}]$. They are defined by the following equations:

$$L_{r,r+1}\mathbf{V^{\star}_{r,r+1}} \cdot \mathbf{N_{r,r+1}} = \int_{M_r}^{M_{r+1}} \mathbf{V} \cdot \mathbf{N}\, \mathrm{d}l,$$

(3.2)
$$L_{r,r+1}\mathbf{P^{\star}_{r,r+1}}\mathbf{N_{r,r+1}} = \int_{M_r}^{M_{r+1}} P\mathbf{N}\, \mathrm{d}l,$$

$$L_{r,r+1}(P\mathbf{V})^{\star}_{r,r+1} \cdot \mathbf{N_{r,r+1}} = \int_{M_r}^{M_{r+1}} P\mathbf{V} \cdot \mathbf{N}\, \mathrm{d}l.$$

With this notation the previous system is now written in the following manner:

(3.3 i)
$$m_i \frac{d}{dt}\tau_i - \sum_{r=1}^{R(i)} L_{r,r+1}\mathbf{V^{\star}_{r,r+1}} \cdot \mathbf{N_{r,r+1}} = 0,$$

(3.3 ii)
$$m_i \frac{d}{dt}\mathbf{V_i} + \sum_{r=1}^{R(i)} L_{r,r+1}P^{\star}_{r,r+1}\mathbf{N_{r,r+1}} = \mathbf{0},$$

(3.3 iii)
$$m_i \frac{d}{dt}E_i + \sum_{r=1}^{R(i)} L_{r,r+1}(P\mathbf{V})^{\star}_{r,r+1} \cdot \mathbf{N_{r,r+1}} = 0.$$

We notice that with this Lagrangian discretization we have to take into account the cell motion. For this purpose we write the node motion equation using the trajectory equation

(3.4)
$$\frac{d}{dt}X_r = u^{\star}_r, \quad X_r(0) = x_r,$$

$$\frac{d}{dt}Y_r = v^{\star}_r, \quad Y_r(0) = y_r,$$

where $(u^{\star}_r, v^{\star}_r)$ are the components of the velocity $\mathbf{V^{\star}_r}$ of the vertex M_r.

In order to complete the space approximation, the following important problems arise:

1. How do we compute the face fluxes defined by (3.2)?
2. How do we compute the node velocities $\mathbf{V^{\star}_r}$?
3. These velocities being known, how can we ensure the compatibility between the mesh motion and the volume variation of the cells?

Thus, our task consists in building a numerical solver that can compute the fluxes $\mathbf{V^{\star}_{r,r+1}}$, $P^{\star}_{r,r+1}$, and $(P\mathbf{V})^{\star}_{r,r+1}$ but also the node velocities $\mathbf{V^{\star}_r}$. Moreover, this must be done coherently. We resolve these questions in the next sections.

3.2. Approximation of the volume equation. Using a geometrical interpretation of (3.3 ii), we can link the volume flux $V^\star_{r,r+1} \cdot N_{r,r+1}$ to the node velocity $V^\star_r$.

First, we notice that $m_i \tau_i = \mathcal{A}_i$, where $\mathcal{A}_i$ is the area of the cell Ω_i. Thus, (3.3 ii) provides the time variation of $\mathcal{A}_i$,

$$(3.5) \qquad \frac{d}{dt}\mathcal{A}_i = \sum_{r=1}^{R(i)} L_{r,r+1} V^\star_{r,r+1} \cdot N_{r,r+1}.$$

The area of the cell Ω_i can also be evaluated from the location of the vertices M_r using the relation (see [28])

$$\mathcal{A}_i = \frac{1}{2} \sum_{r=1}^{R(i)} OM_r \times OM_{r+1} \cdot e_Z.$$

This amounts to summing the area of the triangles (O, M_r, M_{r+1}) (see Figure 3.1) over all the vertices of the cell. Using the coordinates of the vertices and after time differentiation, we get

$$\frac{d}{dt}\mathcal{A}_i = \frac{1}{2} \sum_{r=1}^{R(i)} \left(Y_{r+1} \frac{d}{dt}X_r - X_{r+1}\frac{d}{dt}Y_r + X_r\frac{d}{dt}Y_{r+1} - Y_r\frac{d}{dt}X_{r+1} \right).$$

We rearrange the last two terms of the sum using the transformation $r \to r - 1$ and the periodicity of the indices and get

$$\frac{d}{dt}\mathcal{A}_i = \frac{1}{2} \sum_{r=1}^{R(i)} \left[(Y_{r+1} - Y_r + Y_r - Y_{r-1}) \frac{d}{dt}X_r - (X_{r+1} - X_r + X_r - X_{r-1}) \frac{d}{dt}Y_r \right].$$

This formula can be rewritten as

$$(3.6) \qquad \frac{d}{dt}\mathcal{A}_i = \frac{1}{2} \sum_{r=1}^{R(i)} V^\star_r \cdot (L_{r-1,r}N_{r-1,r} + L_{r,r+1}N_{r,r+1}),$$

and using the change of indices $r - 1 \to r$ for the first term of the sum, we have the equivalent formulation

$$(3.7) \qquad \frac{d}{dt}\mathcal{A}_i = \sum_{r=1}^{R(i)} \frac{1}{2}L_{r,r+1} \left(V^\star_r + V^\star_{r+1} \right) \cdot N_{r,r+1}.$$

The comparison between (3.5) and (3.7) enables us to give the face velocities in term of the vertex velocities, namely,

$$(3.8) \qquad V^\star_{r,r+1} = \frac{1}{2} \left(V^\star_r + V^\star_{r+1} \right).$$

This fundamental relation enables us to write two equivalent discretizations of the specific volume variation. It can be given in terms of the flux through the faces, or equivalently, in term of vertex fluxes. Moreover, the two discretizations are *compatible* with the node motion. We get one of the results of [9], but with a much simpler geometrical argument. We note that (3.8) is consistent with the assumption that the velocity field is linear along face $[M_r, M_{r+1}]$.

Hence, one can consider two methods for computing the face velocities:

- The first one relies on the evaluation of the normal velocity $V_{r,r+1}^\star \cdot N_{r,r+1}$ using a one-dimensional Riemann solver at faces. The vertex velocities $V_r^\star$ have to be computed by solving a linear system built from (3.8) written for all the faces. This system is in general singular, which is why we give up this approach and shall adopt a more robust method.
- In the second method, the velocities $V_r^\star$ are first evaluated using some still-to-be-defined solver. The face velocities are then computed from (3.8). This is the technique we will use in what follows because this method will guarantee the compatibility between vertex motion and cell area variation.

3.3. Approximation of momentum flux. Following the same methodology, we approximate the momentum flux defined at the vertices in such a way that it is compatible with the approximation at faces. Thus, similarly to (3.8) we set

$$(3.9) \qquad P_{r,r+1}^{\star,i} = \frac{1}{2}\left(P_{r,r+\frac{1}{2}}^{\star,i} + P_{r+\frac{1}{2},r+1}^{\star,i}\right),$$

where $P_{r,r+\frac{1}{2}}^{\star,i}$ (resp., $P_{r+\frac{1}{2},r+1}^{\star,i}$) represents the pressure on the half-face $[M_r, M_{r+\frac{1}{2}}]$ (resp., $[M_{r+\frac{1}{2}}, M_{r+1}]$) seen from the cell Ω_i; see Figure 3.2. We have added the superscript i to remove any possible ambiguity. Hence, $\frac{1}{2}L_{r,r+1}P_{r,r+\frac{1}{2}}^{\star,i}N_{r,r+1}$ represents the momentum flux for half-face $[M_r, M_{r+\frac{1}{2}}]$ seen from the cell Ω_i. We observe that at node M_r, seen from the cell Ω_i, there exist two pressures: $P_{r,r+\frac{1}{2}}^{\star,i}$ and $P_{r-\frac{1}{2},r}^{\star,i}$. Because of this, our approach is different from that of [9], where only one pressure is defined at the vertex M_r.
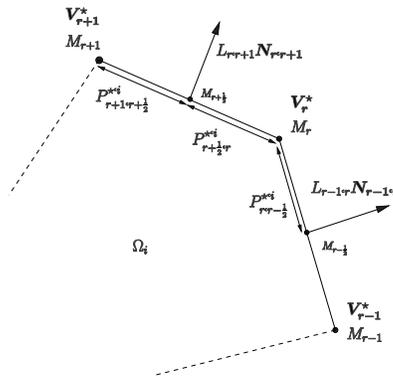

FIG. 3.2. *Pressures at faces.*

Using this definition, the equation for momentum (3.3 iii) is written as

$$(3.10) \qquad m_i\frac{d}{dt}V_i + \sum_{r=1}^{R(i)}\frac{1}{2}L_{r,r+1}\left(P_{r,r+\frac{1}{2}}^{\star,i} + P_{r+\frac{1}{2},r+1}^{\star,i}\right)N_{r,r+1} = 0.$$

If we shift the index r (i.e., $r \to r-1$) in the second term of the summation, we get

$$(3.11) \qquad m_i\frac{d}{dt}V_i + \sum_{r=1}^{R(i)}\frac{1}{2}\left(L_{r-1,r}P_{r-\frac{1}{2},r}^{\star,i}N_{r-1,r} + L_{r,r+1}P_{r,r+\frac{1}{2}}^{\star,i}N_{r,r+1}\right) = 0.$$

It amounts to summing the fluxes over all nodes of the cell. Equations (3.10) and (3.11) are equivalent discretizations. They use either face fluxes or vertex fluxes. The evaluation of these fluxes uses two pressures at a face or at a node for cell Ω_i.

Remark 1. We notice that in the case of a one-dimensional Riemann solver at faces, as classically done, only one single pressure is computed for $[M_r, M_{r+1}]$. The conservation of the momentum is a simple consequence of this approximation. Here, this is no longer the case. In fact, if the cell Ω_j shares face $[M_r, M_{r+1}]$ with Ω_i, the pressures on this face seen from Ω_i may be in general different from those seen from Ω_j. That is why we have put the superscript denoting the cell in the definition of edge pressures. This is an important fact, which is one of the key points of our construction: in adding degrees of freedom as here, we will see later in the text that this enables us to build a node solver which simultaneously provides us with the node velocity and the local conservation of momentum and energy.

3.4. Approximation of the energy flux. In order to get an equivalent discretization in terms of face and nodal fluxes for the total energy equation, we set

$$(3.12) \qquad (P\boldsymbol{V})^{\star,i}_{r,r+1} = \frac{1}{2}\left(P^{\star,i}_{r,r+\frac{1}{2}}\boldsymbol{V}^{\star}_{\boldsymbol{r}} + P^{\star,i}_{r+\frac{1}{2},r+1}\boldsymbol{V}^{\star}_{\boldsymbol{r+1}}\right).$$

Using (3.12), the total energy equation in its face flux formulation is written as

$$(3.13) \qquad m_i\frac{d}{dt}E_i + \sum_{r=1}^{R(i)}\frac{1}{2}L_{r,r+1}\left(P^{\star,i}_{r,r+\frac{1}{2}}\boldsymbol{V}^{\star}_{\boldsymbol{r}} + P^{\star,i}_{r+\frac{1}{2},r+1}\boldsymbol{V}^{\star}_{\boldsymbol{r+1}}\right)\cdot\boldsymbol{N}_{r,r+1} = 0.$$

Shifting once more the index r in the second term of the sum, we get the node flux formulation

$$(3.14) \qquad m_i\frac{d}{dt}E_i + \sum_{r=1}^{R(i)}\frac{1}{2}\left(L_{r-1,r}P^{\star,i}_{r-\frac{1}{2},r}\boldsymbol{N}_{\boldsymbol{r-1,r}} + L_{r,r+1}P^{\star,i}_{r,r+\frac{1}{2}}\boldsymbol{N}_{\boldsymbol{r,r+1}}\right)\cdot\boldsymbol{V}^{\star}_{\boldsymbol{r}} = 0.$$

3.5. Summary. We obtain an approximation of the Euler equations written in Lagrangian coordinates which relies on approximated vertex fluxes:

$$m_i\frac{d}{dt}\tau_i - \sum_{r=1}^{R(i)}\frac{1}{2}\left(L_{r-1,r}\boldsymbol{N}_{\boldsymbol{r-1,r}} + L_{r,r+1}\boldsymbol{N}_{\boldsymbol{r,r+1}}\right)\cdot\boldsymbol{V}^{\star}_{\boldsymbol{r}} = 0,$$

$$(3.15) \qquad m_i\frac{d}{dt}\boldsymbol{V_i} + \sum_{r=1}^{R(i)}\frac{1}{2}\left(L_{r-1,r}P^{\star,i}_{r-\frac{1}{2},r}\boldsymbol{N}_{\boldsymbol{r-1,r}} + L_{r,r+1}P^{\star,i}_{r,r+\frac{1}{2}}\boldsymbol{N}_{\boldsymbol{r,r+1}}\right) = \boldsymbol{0},$$

$$m_i\frac{d}{dt}E_i + \sum_{r=1}^{R(i)}\frac{1}{2}\left(L_{r-1,r}P^{\star,i}_{r-\frac{1}{2},r}\boldsymbol{N}_{\boldsymbol{r-1,r}} + L_{r,r+1}P^{\star,i}_{r,r+\frac{1}{2}}\boldsymbol{N}_{\boldsymbol{r,r+1}}\right)\cdot\boldsymbol{V}^{\star}_{\boldsymbol{r}} = 0.$$

The system (3.15) is equivalent to (3.3) provided that the face fluxes are defined by

$$\boldsymbol{V}^{\star}_{\boldsymbol{r,r+1}} = \tfrac{1}{2}\left(\boldsymbol{V}^{\star}_{\boldsymbol{r}} + \boldsymbol{V}^{\star}_{\boldsymbol{r+1}}\right),$$

$$(3.16) \qquad P^{\star,i}_{r,r+1} = \tfrac{1}{2}\left(P^{\star,i}_{r,r+\frac{1}{2}} + P^{\star,i}_{r+\frac{1}{2},r+1}\right),$$

$$(P\boldsymbol{V})^{\star,i}_{r,r+1} = \tfrac{1}{2}\left(P^{\star,i}_{r,r+\frac{1}{2}}\boldsymbol{V}^{\star}_{\boldsymbol{r}} + P^{\star,i}_{r+\frac{1}{2},r+1}\boldsymbol{V}^{\star}_{\boldsymbol{r+1}}\right).$$

Moreover, this definition is coherent with the vertex motion.

Now, we are going to show how to compute, for each vertex M_r, the velocity $\boldsymbol{V_r^\star}$ and the pressures $P_{r-\frac{1}{2},r}^{\star,i}$ and $P_{r,r+\frac{1}{2}}^{\star,i}$.

4. Construction of a solver at the vertices. The evaluation of $\boldsymbol{V_r^\star}$, $P_{r-\frac{1}{2},r}^{\star,i}$, and $P_{r,r+\frac{1}{2}}^{\star,i}$ relies on the following arguments:
- the global conservation of momentum,
- a local entropy inequality.

The first argument is a consequence of Remark 1: the pressure on the face $[M_r, M_{r+1}]$ is not unique, contrary to the standard finite volume approach. Thus, we lose the automatic conservation of momentum and total energy. Of course, we must guarantee the conservation of momentum and total energy, so we have to add additional constraints on $\boldsymbol{V_r^\star}$, $P_{r-\frac{1}{2},r}^{\star,i}$, and $P_{r,r+\frac{1}{2}}^{\star,i}$.

The second argument is about the thermodynamical consistency of the scheme, which is necessary for a correct computation of the discontinuities. We will build a sufficient condition which will supply a local dissipation of entropy.

The two sets of constraints (conservation and dissipation of entropy) will lead, as we shall see in this section, to a linear system whose unique solution will give us $\boldsymbol{V_r^\star}$, $P_{r-\frac{1}{2},r}^{\star,i}$, and $P_{r,r+\frac{1}{2}}^{\star,i}$.

4.1. Notation around a vertex. In order to exhibit conservation equations for momentum and total energy around a node, let us introduce some new notation. We denote by M_q a generic internal vertex of the mesh, for $q = 1, \ldots, Q$, where Q is the total number of internal nodes. The case of the nodes located on the boundary $\partial\Omega$ will be treated in section 4.7. There are $K(q)$ cells around M_q which are denoted by Ω_k; see Figure 4.1. For the cell Ω_k we denote by $[M_q, M_k]$ and $[M_q, M_{k+1}]$ the edges coming from node M_q. The outward normal to these edges are $\boldsymbol{N_k^k}$, $\boldsymbol{N_{k+1}^k}$ and their lengths L_k, L_{k+1}. Let $\boldsymbol{V_q^\star}$ be the velocity of node M_q and $P_{q,k}^{\star,k}$ (resp., $P_{q,k+1}^{\star,k}$), the half-pressures on edge $[M_q, M_k]$ (resp., $[M_q, M_{k+1}]$) seen from cell Ω_k.

4.2. Conservation relations. Omitting the boundary conditions and summing (3.11) on each cell of the domain, we make a global balance of momentum

$$\frac{d}{dt}\left(\sum_{i=1}^{I} m_i \boldsymbol{V_i}\right) = -\sum_{i=1}^{I}\sum_{r=1}^{r(i)} \frac{1}{2}\left(L_{r-1,r}^i P_{r-\frac{1}{2},r}^{\star,i} \boldsymbol{N_{r-1,r}^i} + L_{r,r+1}^i P_{r,r+\frac{1}{2}}^{\star,i} \boldsymbol{N_{r,r+1}^i}\right).$$
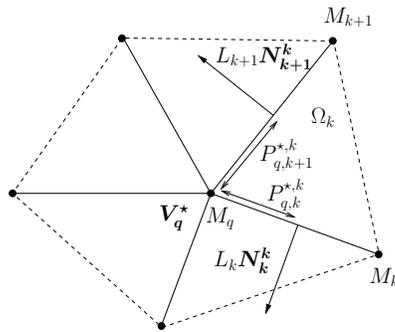

FIG. 4.1. *Notation around the vertex M_q.*

We have added the superscript i for the lengths and normals in order to remove any possible ambiguity. If we replace the global summation over cells by a global summation over nodes, using the notation previously defined, we can rewrite the right-hand side in the following way:

$$\frac{d}{dt}\left(\sum_{i=1}^{I} m_i \boldsymbol{V_i}\right) = -\sum_{q=1}^{Q}\sum_{k=1}^{K(q)} \frac{1}{2}\left(L_k P_{q,k}^{\star,k} \boldsymbol{N_k^k} + L_{k+1} P_{q,k+1}^{\star,k} \boldsymbol{N_{k+1}^k}\right).$$

The (global) conservation of momentum is satisfied provided that the right-hand side vanishes. A sufficient condition is

(4.1)
$$\sum_{k=1}^{K(q)} \frac{1}{2}\left(L_k P_{q,k}^{\star,k} \boldsymbol{N_k^k} + L_{k+1} P_{q,k+1}^{\star,k} \boldsymbol{N_{k+1}^k}\right) = \boldsymbol{0}.$$

This summation is done over all the cells k surrounding vertex M_q; see Figure 4.1. The relation (4.1) can be interpreted as the local equilibrium of vertex M_q under pressure forces. This is also a local conservation relation.

It can be checked that condition (4.1) also implies the global conservation of total energy. To do so, we sum (3.14) on each cell, switch the summation for the cells' and the vertices' indices, and get

$$\frac{d}{dt}\left(\sum_{i=1}^{I} m_i E_i\right) = -\sum_{q=1}^{Q}\sum_{k=1}^{K(q)} \frac{1}{2}\left(L_k P_{q,k}^{\star,k} \boldsymbol{N_k^k} + L_{k+1} P_{q,k+1}^{\star,k} \boldsymbol{N_{k+1}^k}\right) \cdot \boldsymbol{V_q^\star} = 0,$$

using (4.1) and because the velocity $\boldsymbol{V_q^\star}$ is single valued at M_q.

The conservation of volume is easily checked. To do so, we sum the first equation of (3.15) for each cell:

$$\frac{d}{dt}\left(\sum_{i=1}^{I} m_i \tau_i\right) = \sum_{q=1}^{Q}\sum_{k=1}^{K(q)} \frac{1}{2}\left(L_k \boldsymbol{N_k^k} + L_{k+1} \boldsymbol{N_{k+1}^k}\right) \cdot \boldsymbol{V_q^\star}.$$

We know that

(4.2)
$$\sum_{k=1}^{K(q)} \frac{1}{2}\left(L_k \boldsymbol{N_k^k} + L_{k+1} \boldsymbol{N_{k+1}^k}\right) = \boldsymbol{0},$$

since the polygon whose vertices are M_k, $k = 1, \dots, K(q)$, is closed (dotted line in Figure 4.1).

4.3. Entropy inequality. We first compute the time variation of entropy in cell Ω_i. Let us denote it by σ_i. If T_i is the cell average temperature, we have

(4.3)
$$m_i T_i \frac{d}{dt}\sigma_i = m_i\left(\frac{d}{dt}\varepsilon_i + P_i \frac{d}{dt}\tau_i\right).$$

This quantity is evaluated in two steps. First, we compute the variation of internal energy $\frac{d}{dt}\varepsilon_i = \frac{d}{dt}E_i - \boldsymbol{V_i} \cdot \frac{d}{dt}\boldsymbol{V_i}$, and then we evaluate the pressure work $P_i \frac{d}{dt}\tau_i$.

- Internal energy: we dot-multiply (3.11) by $\boldsymbol{V_i}$ to get the kinetic energy variation:

(4.4)
$$m_i \boldsymbol{V_i} \cdot \frac{d}{dt}\boldsymbol{V_i} = -\sum_{r=1}^{R(i)} \frac{1}{2}\left(L_{r-1,r} P_{r-\frac{1}{2},r}^{\star,i} \boldsymbol{N_{r-1,r}} + L_{r,r+1} P_{r,r+\frac{1}{2}}^{\star,i} \boldsymbol{N_{r,r+1}}\right) \cdot \boldsymbol{V_i}.$$

Then (4.4) is subtracted from the total energy variation equation and we have

(4.5)
$$m_i \frac{d}{dt} \varepsilon_i = - \sum_{r=1}^{R(i)} \frac{1}{2} \left(L_{r-1,r} P_{r-\frac{1}{2},r}^{\star,i} \boldsymbol{N_{r-1,r}} + L_{r,r+1} P_{r,r+\frac{1}{2}}^{\star,i} \boldsymbol{N_{r,r+1}} \right) \cdot \left(\boldsymbol{V_r^\star} - \boldsymbol{V_i} \right).$$

• Pressure work: we multiply the first relation of (3.15) by P_i:

$$m_i P_i \frac{d}{dt} \tau_i = \sum_{r=1}^{R(i)} \frac{1}{2} \left(L_{r-1,r} P_i \boldsymbol{N_{r-1,r}} + L_{r,r+1} P_i \boldsymbol{N_{r,r+1}} \right) \cdot \boldsymbol{V_r^\star}.$$

An equivalent formulation is

$$(4.6) \quad m_i P_i \frac{d}{dt} \tau_i = \sum_{r=1}^{R(i)} \frac{1}{2} \left(L_{r-1,r} P_i \boldsymbol{N_{r-1,r}} + L_{r,r+1} P_i \boldsymbol{N_{r,r+1}} \right) \cdot \left(\boldsymbol{V_r^\star} - \boldsymbol{V_i} \right).$$

Knowing that,

$$\sum_{r=1}^{R(i)} \frac{1}{2} \left(L_{r-1,r} \boldsymbol{N_{r-1,r}} + L_{r,r+1} \boldsymbol{N_{r,r+1}} \right) = \boldsymbol{0},$$

because the boundary of Ω_i is a closed polygon.

Last, the summation of (4.5) and (4.6) gives

$$m_i T_i \frac{d}{dt} \sigma_i = \sum_{r=1}^{R(i)} \frac{1}{2} \left[L_{r-1,r} \left(P_i - P_{r-\frac{1}{2},r}^{\star,i} \right) \boldsymbol{N_{r-1,r}} + L_{r,r+1} \left(P_i - P_{r,r+\frac{1}{2}}^{\star,i} \right) \boldsymbol{N_{r,r+1}} \right]$$
$$\cdot \left(\boldsymbol{V_r^\star} - \boldsymbol{V_i} \right).$$

A sufficient condition for the right-hand side of this relation to be positive is

$$(4.7) \quad \begin{cases} P_i - P_{r-\frac{1}{2},r}^{\star,i} = \alpha_i \left(\boldsymbol{V_r^\star} - \boldsymbol{V_i} \right) \cdot \boldsymbol{N_{r-1,r}}, \quad r = 1, \dots, R(i), \\[2mm] P_i - P_{r,r+\frac{1}{2}}^{\star,i} = \alpha_i \left(\boldsymbol{V_r^\star} - \boldsymbol{V_i} \right) \cdot \boldsymbol{N_{r,r+1}}, \quad r = 1, \dots, R(i), \end{cases}$$

where α_i is a positive coefficient that has the dimension of a mass flux. These two relations can be interpreted as (discretized) Riemann invariants along the directions $\boldsymbol{N_{r-1,r}}$ and $\boldsymbol{N_{r,r+1}}$. Our main motivation is to recover the approximate acoustic solver [24] for one-dimensional flows, which is why the parameter α_i is set to the value

$$(4.8) \qquad\qquad\qquad \alpha_i = \rho_i c_i,$$

where $c_i = \sqrt{\left(\frac{\partial P}{\partial \rho} \right)_\sigma}$ represents the isentropic sound speed. Under condition (4.7), the variation of entropy is

(4.9)
$$m_i T_i \frac{d}{dt} \sigma_i = \sum_{r=1}^{R(i)} \frac{1}{2} \rho_i c_i \left\{ L_{r-1,r} \left[\left(\boldsymbol{V_r^\star} - \boldsymbol{V_i} \right) \cdot \boldsymbol{N_{r-1,r}} \right]^2 + L_{r,r+1} \left[\left(\boldsymbol{V_r^\star} - \boldsymbol{V_i} \right) \cdot \boldsymbol{N_{r,r+1}} \right]^2 \right\}.$$
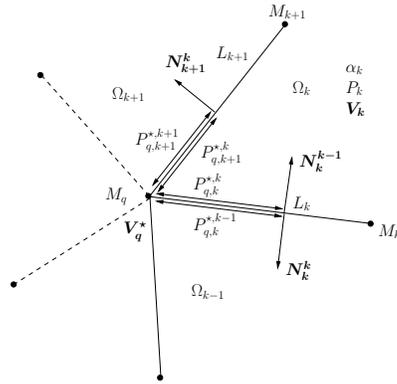
FIG. 4.2. *States around internal node M_q.*

Remark 2. The relation (4.9) is very similar to the entropy production term resulting from a two-dimensional linear artificial viscosity term; see [5]. We notice that (4.9) implies a positive production of entropy, even in the case of isentropic flows. For such flows our scheme does not conserve entropy. This is typical for Godunov-type schemes. If we rewrite the sufficient condition (4.7) using notation around a generic vertex M_q, we obtain

$$(4.10) \quad \begin{cases} P_k - P_{q,k}^{\star,k} = \alpha_k \left(\boldsymbol{V_q^\star} - \boldsymbol{V_k} \right) \cdot \boldsymbol{N_k^k}, & k = 1, \dots, K(q), \\[2mm] P_k - P_{q,k+1}^{\star,k} = \alpha_k \left(\boldsymbol{V_q^\star} - \boldsymbol{V_k} \right) \cdot \boldsymbol{N_{k+1}^k}, & k = 1, \dots, K(q), \end{cases}$$

where α_k, P_k, and $\boldsymbol{V_k}$ stand for acoustic impedance, pressure, and velocity in cell Ω_k. We point out that for a vertex M_q (not on the boundary of the computational domain), we have to compute $2K(q)$ pressures, that is, together with the velocity $\boldsymbol{V_q^\star}$, to evaluate $2K(q) + 2$ scalar unknowns. Equation (4.1) provides 2 scalar relations, and (4.10) gives $2K(q)$ more. Hence, we can compute the pressures and the velocity at the vertex M_q. This is the topic of the next section.

4.4. Evaluation of the velocity and pressures at the vertices. Using sufficient conditions (4.1) and (4.10), we write the linear system satisfied by the components of the velocity $\boldsymbol{V_q^\star}$ of an internal vertex M_q. This generic vertex is not on the boundary of the domain, so that it is surrounded by the cells Ω_k, $k = 1, \dots, K(q)$; see Figure 4.2. With this new notation, if we shift index ($k \to k-1$) in the second term of (4.1), we get

$$(4.11) \quad \sum_{k=1}^{K(q)} L_k \left(P_{q,k}^{\star,k} - P_{q,k}^{\star,k-1} \right) \boldsymbol{N_k^{k-1}} = \boldsymbol{0},$$

where we have used $\boldsymbol{N_k^k} = -\boldsymbol{N_k^{k-1}}$. We proceed in the same way for (4.10):

$$(4.12) \quad \begin{cases} P_{q,k}^{\star,k} = P_k + \alpha_k \left(\boldsymbol{V_q^\star} - \boldsymbol{V_k} \right) \cdot \boldsymbol{N_k^{k-1}}, \\[2mm] P_{q,k}^{\star,k-1} = P_{k-1} - \alpha_{k-1} \left(\boldsymbol{V_q^\star} - \boldsymbol{V_{k-1}} \right) \cdot \boldsymbol{N_k^{k-1}}. \end{cases}$$

After substitution of (4.12) into (4.11), we obtain the following equation satisfied by $\boldsymbol{V_q^\star}$:

(4.13)

$$\sum_{k=1}^{K(q)} L_k \left(\alpha_{k-1} + \alpha_k\right)$$

$$\times \left[\boldsymbol{V_q^\star} \cdot \boldsymbol{N_k^{k-1}} - \frac{P_{k-1} - P_k + \alpha_{k-1}\boldsymbol{V_{k-1}} \cdot \boldsymbol{N_k^{k-1}} + \alpha_k \boldsymbol{V_k} \cdot \boldsymbol{N_k^{k-1}}}{\alpha_{k-1} + \alpha_k} \right] \boldsymbol{N_k^{k-1}} = \boldsymbol{0}.$$

If we set

$$\mathcal{V}_k^\star = \frac{P_{k-1} - P_k + \alpha_{k-1}\boldsymbol{V_{k-1}} \cdot \boldsymbol{N_k^{k-1}} + \alpha_k \boldsymbol{V_k} \cdot \boldsymbol{N_k^{k-1}}}{\alpha_{k-1} + \alpha_k},$$

$\mathcal{V}_k^\star$ is the normal velocity given by the classical one-dimensional acoustic Riemann solver for face $[M_q, M_k]$. With this notation, we can rewrite (4.13) and give an interesting interpretation of it:

$$\sum_{k=1}^{K(q)} L_k \left(\alpha_{k-1} + \alpha_k\right) \left[\boldsymbol{V_q^\star} \cdot \boldsymbol{N_k^{k-1}} - \mathcal{V}_k^\star \right] \boldsymbol{N_k^{k-1}} = \boldsymbol{0}.$$

A straightforward calculation shows that the left-hand side of this last equation is the gradient of the following quadratic functional:

(4.14)
$$F(u_q^\star, v_q^\star) = \sum_{k=1}^{K(q)} L_k \left(\alpha_{k-1} + \alpha_k\right) \left[\boldsymbol{V_q^\star} \cdot \boldsymbol{N_k^{k-1}} - \mathcal{V}_k^\star \right]^2,$$

where $(u_q^\star, v_q^\star)$ denotes the components of $\boldsymbol{V_q^\star}$. Consequently, the solution of (4.13) reaches the minimum of the functional $F(u_q^\star, v_q^\star)$. Hence, it appears that the nodal velocity $\boldsymbol{V_q^\star}$ is obtained from *a weighted least squares procedure*. This least squares procedure corresponds to the overdetermined system equating the projection of the nodal velocity onto the edge normal N_k^{k-1} with the normal velocity $\mathcal{V}_k^\star$ obtained from the acoustic approximate Riemann solver. For each edge impinging on node M_q, the weight is $L_k(\alpha_{k-1} + \alpha_k)$.

Finally, we write the 2×2 linear system satisfied by $(u_q^\star, v_q^\star)$:

(4.15)
$$\begin{cases} A u_q^\star + C v_q^\star = SM_X, \\ C u_q^\star + B v_q^\star = SM_Y, \end{cases}$$

where A, B, and C are defined by

$$A = \sum_{k=1}^{K(q)} L_k \left(\alpha_{k-1} + \alpha_k\right) \left(N_{k,X}^{k-1}\right)^2,$$

$$B = \sum_{k=1}^{K(q)} L_k \left(\alpha_{k-1} + \alpha_k\right) \left(N_{k,Y}^{k-1}\right)^2,$$

$$C = \sum_{k=1}^{K(q)} L_k \left(\alpha_{k-1} + \alpha_k\right) N_{k,X}^{k-1} N_{k,Y}^{k-1}.$$

Here, $(N_{k,X}^{k-1}, N_{k,Y}^{k-1})$ are the coordinates of $\boldsymbol{N}_k^k$. The right-hand side (SM_X, SM_Y) of (4.15) are the components of the vector $\boldsymbol{SM}$ defined by

$$\boldsymbol{SM} = \sum_{k=1}^{K(q)} L_k \left(\alpha_{k-1} + \alpha_k\right) \mathcal{V}_k^{\star} \boldsymbol{N}_{\boldsymbol{k}}^{\boldsymbol{k-1}}.$$

The determinant Δ of (4.15) is $\Delta = AB - C^2$. We show that it is always positive. In order to simplify notation, let us introduce $\beta_k = \sqrt{L_k \left(\alpha_{k-1} + \alpha_k\right)}$ and $\boldsymbol{N_k} = \boldsymbol{N}_{\boldsymbol{k}}^{\boldsymbol{k-1}}$ for $k = 1, \ldots, K(q)$. We define

$$\boldsymbol{U_X} = (\beta_1 N_{1,X}, \ldots, \beta_K N_{K,X})^t ,$$
$$\boldsymbol{U_Y} = (\beta_1 N_{1,Y}, \ldots, \beta_K N_{K,Y})^t .$$

We have immediately $A = \|\boldsymbol{U_X}\|^2$, $B = \|\boldsymbol{U_Y}\|^2$, and $C = \langle \boldsymbol{U_X}, \boldsymbol{U_Y} \rangle$, where $\langle , \rangle$ is the inner scalar product of $\mathbb{R}^K$ and $\| \ \|$ its associated norm. From the Cauchy–Schwarz inequality, we know that $\Delta \geq 0$. In fact, $\Delta = 0$ if and only if one of the two vectors is null or $\boldsymbol{U_X}$ and $\boldsymbol{U_Y}$ are colinear. This situation is generally impossible unless the edges around the node merge into a single line.

We have shown that the system (4.15) always has a unique solution which determines the velocity $\boldsymbol{V_q^{\star}}$. From (4.12), we can get the pressures $P_{q,k}^{\star,k}$ and $P_{q,k}^{\star,k-1}$. Moreover, this nodal solver is invariant under translation, homothety, and rotation of center M_q.

Remark 3. If the flow is uniform (i.e., with a uniform velocity $\boldsymbol{V}^0$ and pressure P^0), we can easily check that the solution of (4.15) reduces to $\boldsymbol{V}_q^{\star} = \boldsymbol{V}^0$.

4.5. Summary of the discrete evolution equations. We give in this section the summary of the discrete evolution equations that constitute a closed set of equations for the unknowns $\{\tau_i, \boldsymbol{V_i}, E_i\}$:

$$m_i \frac{d}{dt}\tau_i - \sum_{r=1}^{R(i)} \frac{1}{2} \left(L_{r-1,r} \boldsymbol{N_{r-1,r}} + L_{r,r+1} \boldsymbol{N_{r,r+1}}\right) \cdot \boldsymbol{V_r^{\star}} = 0,$$

(4.16) $$m_i \frac{d}{dt}\boldsymbol{V_i} + \sum_{r=1}^{R(i)} \frac{1}{2} \left(L_{r-1,r} P_{r-\frac{1}{2},r}^{\star,i} \boldsymbol{N_{r-1,r}} + L_{r,r+1} P_{r,r+\frac{1}{2}}^{\star,i} \boldsymbol{N_{r,r+1}}\right) = \boldsymbol{0},$$

$$m_i \frac{d}{dt}E_i + \sum_{r=1}^{R(i)} \frac{1}{2} \left(L_{r-1,r} P_{r-\frac{1}{2},r}^{\star,i} \boldsymbol{N_{r-1,r}} + L_{r,r+1} P_{r,r+\frac{1}{2}}^{\star,i} \boldsymbol{N_{r,r+1}}\right) \cdot \boldsymbol{V_r^{\star}} = 0.$$

We note that these equations have been written using a vertex flux formulation (see section 3). Those fluxes are obtained via a nodal solver which is derived in section 4. The edge pressures $P_{r-\frac{1}{2},r}^{\star,i}, P_{r,r+\frac{1}{2}}^{\star,i}$ are computed as follows:

(4.17)
$$\begin{cases} P_i - P_{r-\frac{1}{2},r}^{\star,i} = \rho_i c_i \left(\boldsymbol{V_r^{\star}} - \boldsymbol{V_i}\right) \cdot \boldsymbol{N_{r-1,r}}, & r = 1, \ldots, R(i), \\[2mm] P_i - P_{r,r+\frac{1}{2}}^{\star,i} = \rho_i c_i \left(\boldsymbol{V_r^{\star}} - \boldsymbol{V_i}\right) \cdot \boldsymbol{N_{r,r+1}}, & r = 1, \ldots, R(i). \end{cases}$$

If q denotes the global index corresponding to the local index r, the nodal velocity $\boldsymbol{V_r^{\star}} \equiv \boldsymbol{V_q^{\star}} = (u_q^{\star}, v_q^{\star})$ is given by the solution of the 2×2 linear system

(4.18)
$$\begin{cases} Au_q^{\star} + Cv_q^{\star} = SM_X, \\ Cu_q^{\star} + Bv_q^{\star} = SM_Y, \end{cases}$$

where A, B, and C are defined by

$$A = \sum_{k=1}^{K(q)} L_k \left(\rho_{k-1} c_{k-1} + \rho_k c_k \right) \left(N_{k,X}^{k-1} \right)^2,$$

$$B = \sum_{k=1}^{K(q)} L_k \left(\rho_{k-1} c_{k-1} + \rho_k c_k \right) \left(N_{k,Y}^{k-1} \right)^2,$$

$$C = \sum_{k=1}^{K(q)} L_k \left(\rho_{k-1} c_{k-1} + \rho_k c_k \right) N_{k,X}^{k-1} N_{k,Y}^{k-1},$$

where the index k denotes the label of the cells (edges) that surround the node M_q; see Figure 4.2. The right-hand side of (4.18), $\boldsymbol{SM} = (SM_X, SM_Y)^t$, is given by

$$\boldsymbol{SM} = \sum_{k=1}^{K(q)} L_k \left(\rho_{k-1} c_{k-1} + \rho_k c_k \right) \mathcal{V}_k^\star \boldsymbol{N_k^{k-1}},$$

where $\mathcal{V}_k^\star$ corresponds to the normal velocity given by the classical one-dimensional acoustic Riemann solver

$$\mathcal{V}_k^\star = \frac{P_{k-1} - P_k + \rho_{k-1} c_{k-1} \boldsymbol{V_{k-1}} \cdot \boldsymbol{N_k^{k-1}} + \rho_k c_k \boldsymbol{V_k} \cdot \boldsymbol{N_k^{k-1}}}{\rho_{k-1} c_{k-1} + \rho_k c_k}.$$

Before we detail our implementation of the boundary conditions, we provide in the next section an interpretation of our results in the case of a one-dimensional flow with a planar symmetry and in the case of a flow with a cylindrical symmetry.

4.6. Interpretation of the solver in two simple cases.

4.6.1. One-dimensional flow with planar symmetry. Let us consider M_q surrounded by four quadrangular cells. They are numbered from 1 to 4 in the counterclockwise direction; see Figure 4.3. We consider the frame $(M_q, \boldsymbol{e_X}, \boldsymbol{e_Y})$. The vector $\boldsymbol{N_k^{k-1}}$ is the normal to the edge shared by cells $k-1$ and k. The length of this edge is L_k. The indexing system is periodic with period 4, and the flow is one-dimensional in the $\boldsymbol{e_X}$ direction so that the velocity field in the cell k reduces to $\boldsymbol{V}_k = u_k \boldsymbol{e_X}$. Moreover, any scalar quantity φ satisfies $\varphi_1 \equiv \varphi_4$ and $\varphi_2 \equiv \varphi_3$. The cells 1 and 4 contain the state defined by P_1, c_1, $\boldsymbol{V_1} = u_1 \boldsymbol{e_X}$. The cells 2 and 3 contain the state defined by P_2, c_2, $\boldsymbol{V_2} = u_2 \boldsymbol{e_X}$. Using this notation, the evaluation of the matrix
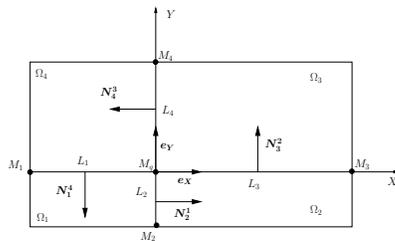

FIG. 4.3. *One-dimensional planar flow.*

coefficients A, B, C is straightforward:

$$A = (L_2 + L_4)(\rho_1 c_1 + \rho_2 c_2),$$

$$B = 2(L_1 \rho_1 c_1 + L_3 \rho_2 c_2),$$

$$C = 0.$$

The calculation of $\boldsymbol{SM}$ gives

$$SM_X = (L_2 + L_4)(P_1 - P_2 + \rho_1 c_1 u_1 + \rho_2 c_2 u_2),$$

$$SM_Y = 0.$$

Therefore $v_q^\star = 0$ and

$$u_q^\star = \frac{P_1 - P_2 + \rho_1 c_1 u_1 + \rho_2 c_2 u_2}{\rho_1 c_1 + \rho_2 c_2}.$$

We recover exactly the acoustic Riemann solver!

4.6.2. One-dimensional flow with cylindrical symmetry. We consider an equiangular cylindrical mesh centered at O. We denote by θ the angle of any sector. The mesh may be nonregular in the radial direction. Any vertex M_q is surrounded by four trapezoidal cells. In order to simplify the algebra, we choose to work in the local orthonormal frame $(M_q, \boldsymbol{e_X}, \boldsymbol{e_Y})$, where $\boldsymbol{e_X}$ is the unit vector colinear to $\boldsymbol{OM_q}$; see Figure 4.4. We use the same conventions as in the previous section. The cells 1 and 4 contain the states defined by P_1, ρ_1, c_1. The cells 2 and 3 contain the states defined by P_2, ρ_2, c_2. Due to cylindrical symmetry, the velocities are defined by $\boldsymbol{V_1} = V_1 \boldsymbol{N_2^1}$, $\boldsymbol{V_2} = V_2 \boldsymbol{N_2^1}$, $\boldsymbol{V_3} = -V_2 \boldsymbol{N_4^3}$, and $\boldsymbol{V_4} = -V_1 \boldsymbol{N_4^3}$. In the frame $(M_q, \boldsymbol{e_X}, \boldsymbol{e_Y})$, the normals are written as

$$\boldsymbol{N_2^1} = \begin{pmatrix} \cos(\theta/2) \\ -\sin(\theta/2) \end{pmatrix}, \quad \boldsymbol{N_2^3} = \begin{pmatrix} 0 \\ 1 \end{pmatrix}, \quad \boldsymbol{N_4^3} = \begin{pmatrix} -\cos(\theta/2) \\ -\sin(\theta/2) \end{pmatrix}, \quad \text{and } \boldsymbol{N_1^4} = \begin{pmatrix} 0 \\ -1 \end{pmatrix}.$$
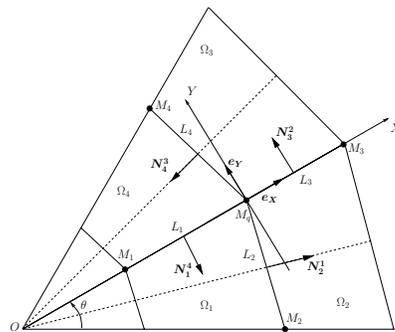
FIG. 4.4. *One-dimensional cylindrical flow.*

After calculations we get

$$
\begin{aligned}
A &= (L_2 + L_4) \cos^2\left(\frac{\theta}{2}\right) (\rho_1 c_1 + \rho_2 c_2), \\
B &= 2L_1 \rho_1 c_1 + (L_2 + L_4) \sin^2\left(\frac{\theta}{2}\right) (\rho_1 c_1 + \rho_2 c_2) + 2L_3 \rho_2 c_2, \\
C &= (L_4 - L_2) \sin\left(\frac{\theta}{2}\right) \cos\left(\frac{\theta}{2}\right) (\rho_1 c_1 + \rho_2 c_2).
\end{aligned}
$$

We also obtain

$$
\boldsymbol{SM} = (P_1 - P_2 + \rho_1 c_1 V_1 + \rho_2 c_2 V_2) \left(\begin{array}{c} (L_2 + L_4) \cos(\theta/2) \\ (L_4 - L_2) \sin(\theta/2) \end{array} \right).
$$

Using the symmetry we have $L_2 = L_4$; thus $C = 0$ and $SM_Y = 0$. Therefore $v_q^\star = 0$, and the velocity is of the form $\boldsymbol{V_q^\star} = u_q^\star \boldsymbol{e_X}$. The evaluation of $u_q^\star$ is straightforward:

$$
u_q^\star = \frac{P_1 - P_2 + \rho_1 c_1 V_1 + \rho_2 c_2 V_2}{\rho_1 c_1 + \rho_2 c_2} \frac{1}{\cos(\frac{\theta}{2})}.
$$

This is once more the acoustic solver modified by a geometrical factor that is a consequence of the projection of $\boldsymbol{V_k}$ on the axis $[O, M_q]$. This term has no consequence since $\cos(\frac{\theta}{2}) \to 1$ when $\theta \to 0$. We also notice that the velocity is radial because the angle between two sectors is uniform. If the mesh does not satisfy this property, therefore $L_2 \neq L_4$ and $C \neq 0$, and consequently, $v_q^\star \neq 0$.

4.7. Boundary conditions. In this section, we explain our implementation of boundary conditions which is consistent with our internal solver. In the Lagrangian formalism, we have to consider two types of boundary conditions on the boundary $\partial\Omega$: either we impose the pressure or we impose the normal component of the velocity. We use the same type of notation as in section 4.1. Let $M_q \in \partial\Omega$. It is surrounded by $K(q) = K$ cells contained in the domain Ω. There are $K + 1$ edges impinging on M_q. They are numbered counterclockwise; see Figure 4.5. The first and last cells Ω_1 and Ω_K have an edge on the boundary $\partial\Omega$. The outward normals to the two boundary edges coming out of M_q are denoted by $-\boldsymbol{N_1^0}$ and $\boldsymbol{N_{K+1}^K}$ coherently with our notation.
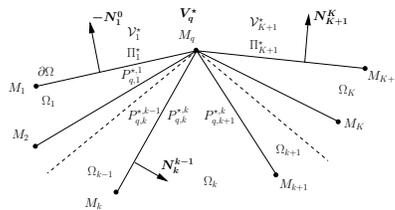

FIG. 4.5. *Notation for the boundary conditions.*

4.7.1. Case of a prescribed pressure. We denote by $\Pi_1^\star$ and $\Pi_{K+1}^\star$ the pressures that are imposed on the boundary edges; see Figure 4.5. We have to compute the $2K$ pressures $P_{q,k}^{\star,k-1}$, $k = 2, \ldots, K + 1$, and $P_{q,k}^{\star,k}$, $k = 1, \ldots, K$; adding the velocity $\boldsymbol{V_q^\star}$ of the vertex M_q, we have a total number of $2K + 2$ scalar unknowns. These unknowns satisfy the previous relations (conservation of momentum, entropy

inequality). For the conservation relation, we make a balance around the vertex M_q by counting the pressure forces due to the boundary conditions. We get

$$(4.19) \quad -L_1 P_{q,1}^{\star,1} \boldsymbol{N_1^0} + \sum_{k=2}^{K} L_k \left(P_{q,k}^{\star,k-1} - P_{q,k}^{\star,k} \right) \boldsymbol{N_k^{k-1}} + L_{K+1} P_{q,K+1}^{\star,K} \boldsymbol{N_{K+1}^K}$$
$$= -L_1 \Pi_1^\star \boldsymbol{N_1^0} + L_{K+1} \Pi_{K+1}^\star \boldsymbol{N_{K+1}^K}.$$

The entropy inequality provides

$$(4.20) \quad P_{q,k}^{\star,k} = P_k + \alpha_k \left(\boldsymbol{V_q^\star} - \boldsymbol{V_k} \right) \cdot \boldsymbol{N_k^{k-1}}, \quad k = 1, \dots, K,$$
$$P_{q,k}^{\star,k-1} = P_{k-1} - \alpha_{k-1} \left(\boldsymbol{V_q^\star} - \boldsymbol{V_{k-1}} \right) \cdot \boldsymbol{N_k^{k-1}}, \quad k = 2, \dots, K+1.$$

The use of (4.20) in (4.19) leads to

$$(4.21) \quad \begin{cases} \tilde{A} u_q^\star + \tilde{C} v_q^\star = \widetilde{SM_X}, \\ \tilde{C} u_q^\star + \tilde{B} v_q^\star = \widetilde{SM_Y}, \end{cases}$$

where the coefficients are

$$\tilde{A} = \sum_{k=2}^{K} L_k \left(\alpha_{k-1} + \alpha_k \right) \left(N_{k,X}^{k-1} \right)^2 + L_1 \alpha_1 \left(N_{1,X}^0 \right)^2 + L_{K+1} \alpha_{K+1} \left(N_{K+1,X}^K \right)^2,$$

$$\tilde{B} = \sum_{k=2}^{K} L_k \left(\alpha_{k-1} + \alpha_k \right) \left(N_{k,Y}^{k-1} \right)^2 + L_1 \alpha_1 \left(N_{1,Y}^0 \right)^2 + L_{K+1} \alpha_{K+1} \left(N_{K+1,Y}^K \right)^2,$$

$$\tilde{C} = \sum_{k=2}^{K} L_k \left(\alpha_{k-1} + \alpha_k \right) N_{k,X}^{k-1} N_{k,Y}^{k-1} + L_1 \alpha_1 N_{1,X}^0 N_{1,Y}^0 + L_{K+1} \alpha_{K+1} N_{K+1,X}^K N_{K+1,Y}^K.$$

We see that we recover the coefficients A, B and C, where the contribution of the boundary faces are now taken into account. The right-hand side of (4.21) is written as

$$\widetilde{\boldsymbol{SM}} = \sum_{k=2}^{K} L_k \left[P_{k-1} - P_k + (\alpha_{k-1} \boldsymbol{V_{k-1}} + \alpha_k \boldsymbol{V_k}) \cdot \boldsymbol{N_{k-1}^k} \right] \boldsymbol{N_{k-1}^k}$$
$$- L_1 \left[P_1 - \Pi_1^\star - \alpha_1 \boldsymbol{V_1} \cdot \boldsymbol{N_1^0} \right] \boldsymbol{N_1^0}$$
$$+ L_{K+1} \left[P_K - \Pi_{K+1}^\star + \alpha_K \boldsymbol{V_K} \cdot \boldsymbol{N_K^{K+1}} \right] \boldsymbol{N_K^{K+1}}.$$

From the Cauchy–Schwartz inequality, we know that $\tilde{C}^2 < \tilde{A}\tilde{B}$. Hence, the linear system (4.21) always has a unique solution $(u_q^\star, v_q^\star)$. The pressures $P_{q,k}^{\star,k-1}, k = 2, \dots, K+1$, and $P_{q,k}^{\star,k}, k = 1, \dots, K$, are obtained from (4.20).

4.7.2. Case of a prescribed normal velocity. Let $\mathcal{V}_1^\star$ and $\mathcal{V}_{K+1}^\star$ be the values of the prescribed normal velocities on the boundary edges coming out of M_q. We distinguish the following two cases:

- $-\boldsymbol{N_1^0}$ and $\boldsymbol{N_K^{K+1}}$ are not colinear: in this case the value of $\boldsymbol{V_q^\star}$ is given by the boundary conditions, and the components of the vertex velocity are the solution of the linear system

$$\begin{cases} -N_{1,X}^0 u_q^\star - N_{1,Y}^0 v_q^\star = \mathcal{V}_1^\star, \\ N_{K,X}^{K+1} u_q^\star + N_{K,Y}^{K+1} v_q^\star = \mathcal{V}_{K+1}^\star. \end{cases}$$

Since the normals are not colinear, this linear system always has a unique solution. The pressures are computed from (4.20).

- $-\boldsymbol{N_1^0}$ and $\boldsymbol{N_K^{K+1}}$ are colinear: in this case, $\boldsymbol{V_q^\star}$ is not given directly, and we need to know the balance of momentum around the vertex M_q which takes the boundary conditions into account:

(4.22)

$$-L_1 P_{q,1}^{\star,1} \boldsymbol{N_1^0} + \sum_{k=2}^{K} L_k \left(P_{q,k}^{\star,k-1} - P_{q,k}^{\star,k} \right) \boldsymbol{N_k^{k-1}} + L_{K+1} P_{q,K+1}^{\star,K} \boldsymbol{N_{K+1}^K}$$
$$= \left(-L_1 \boldsymbol{N_1^0} + L_{K+1} \boldsymbol{N_K^{K+1}} \right) \Pi^\star,$$

where $\Pi^\star$ is an average pressure applied on the external side of the edges coming out of M_q. The pressure $\Pi^\star$ is a new unknown, but we have an additional equation corresponding to the boundary condition

(4.23) $$\left(-L_1 \boldsymbol{N_1^0} + L_{K+1} \boldsymbol{N_K^{K+1}} \right) \cdot \boldsymbol{V_q^\star} = L_1 \mathcal{V}_1^\star + L_{K+1} \mathcal{V}_{K+1}^\star.$$

Using (4.20) in (4.22) combined with (4.23), we get

(4.24)
$$\begin{cases} \tilde{A} u_q^\star + \tilde{C} v_q^\star + D\Pi^\star = \widehat{SM_X}, \\ \tilde{C} u_q^\star + \tilde{B} v_q^\star + E\Pi^\star = \widehat{SM_Y}, \\ D u_q^\star + E v_q^\star = L_1 \mathcal{V}_1^\star + L_{K+1} \mathcal{V}_{K+1}^\star. \end{cases}$$

The coefficients $\tilde{A}$, $\tilde{B}$, and $\tilde{C}$ have already been defined in the previous section and we have set $D = -L_1 N_{1,X}^0 + L_{K+1} N_{K,X}^{K+1}$, $E = -L_1 N_{1,Y}^0 + L_{K+1} N_{K,Y}^{K+1}$. The right-hand side of (4.24) is

$$\widehat{\boldsymbol{SM}} = \sum_{k=2}^{K} L_k \left[P_{k-1} - P_k + (\alpha_{k-1} \boldsymbol{V_{k-1}} + \alpha_k \boldsymbol{V_k}) \cdot \boldsymbol{N_{k-1}^k} \right] \boldsymbol{N_{k-1}^k}$$
$$- L_1 \left[P_1 - \alpha_1 \boldsymbol{V_1} \cdot \boldsymbol{N_1^0} \right] \boldsymbol{N_1^0} + L_{K+1} \left[P_K + \alpha_K \boldsymbol{V_K} \cdot \boldsymbol{N_K^{K+1}} \right] \boldsymbol{N_K^{K+1}}.$$

The determinant of (4.24) is $\Delta = -\tilde{A}E + 2\tilde{C}DE - \tilde{B}D^2$. Using the fact that $|\tilde{C}| < \sqrt{\tilde{A}\tilde{B}}$, one can show that $\Delta < 0$ provided the mesh is not degenerated: (4.24) always admits a unique solution $(u_q^\star, v_q^\star)$, and then we can always define a unique set of pressures due to (4.20).

Remark 4. We have implemented a numerical test in order to determine the colinearity of the unit normal $-\boldsymbol{N_1^0}$ and $\boldsymbol{N_K^{K+1}}$ with a fixed threshold $\varepsilon > 0$. For numerical applications we have set $\varepsilon = 10^{-10}$. Namely, for $|\det(\boldsymbol{N_1^0}, \boldsymbol{N_K^{K+1}})| \leq \varepsilon$, $-\boldsymbol{N_1^0}$ and $\boldsymbol{N_K^{K+1}}$ are almost colinear, and we use the second alternative in order to avoid an ill-conditioned system.

4.8. Some remarks. From conservation arguments and one entropy inequality, we have been able to construct a nodal solver. This scheme shares some characteristics with the method developed in [9] and can be interpreted as a two-dimensional extension of the acoustic solver. It is interesting to realize that we need only the knowledge of the isentropic speed of sound: it is very easy to extend it to more general equation
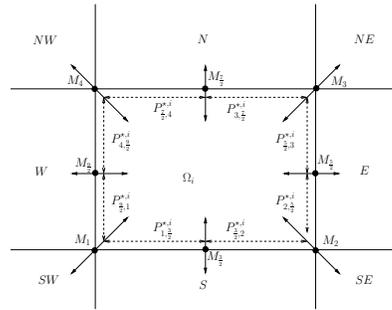
FIG. 4.6. *Stencil for a quadrangular mesh.*

of state. The precise form of the equation of state, analytical or tabulated, does not matter.

We have rigorously shown that the linear system which provides the components of the vertex velocity admits a unique solution, provided that the mesh is not degenerated; see the end of section 4.4. This is also true for vertices located on the boundary, whereas with the method developed in [9] some difficulties have been encountered for vertices located at the corner on the boundary of a rectangular domain.

We have also checked that our solver recovers the one-dimensional acoustic solver in the case of one-dimensional planar and cylindrical flows, contrarily to [9]. More precisely, the calculation of the node velocity with the solver described in [9] gives, for a one-dimensional flow with planar symmetry,

$$u_q^\star = \frac{P_1 - P_2 + \rho_1 c_1 u_1 + \rho_2 c_2 u_2}{\rho_1 c_1 + \rho_2 c_2} \frac{\sqrt{\Delta X^2 + \Delta Y^2}}{\Delta Y},$$

where $L_1 = L_3 = \Delta X$ and $L_2 = L_4 = \Delta Y$ are mesh spacing along directions $\boldsymbol{e_X}$ and $\boldsymbol{e_Y}$. With this nodal solver, one recovers the one-dimensional acoustic solver velocity multiplied by a factor which depends on the aspect ratio of the cells.

Last, our method fully answers the questions raised at the beginning of this paper since it uniquely provides the vertex velocity and the face fluxes. The main new features of our scheme is the introduction of four pressures on each edge, two for each node on each side of the edge, that is, eight pressures at each node for a quadrangular mesh.

We can compute, in a coherent way, the vertex motion as well as the face fluxes. This solver has been constructed delocalizing the fluxes from the faces to the vertices. Consequently, the conservation of momentum and energy is obtained around the node. This implies a fundamental difference with a standard finite volume scheme.

This difference can be illustrated by the consideration of a mesh made of quadrangular cells. We denote by 1, 2, 3, and 4 the vertices of the cell Ω_i and by S, SE, E, NE, N, NW, O, and SW the neighboring cells; see Figure 4.6. In a standard finite volume scheme with an approximate Riemann solver, the cell Ω_i exchanges information only with the neighboring cells having a common face, i.e., the cells S, E, N, and O. This is a 5 point scheme.

With our scheme, the cell Ω_i exchanges momentum and energy with the neighboring cells having a common vertex, i.e., the cells S, SE, E, NE, N, NW, W, and SW. This is a 9 point scheme. The four additional cells reinforce the genuinely multidimensional nature of our scheme.

5. Time discretization. In this section, we time discretize the system that describes the evolution of the physical variables $(\tau_i, \boldsymbol{V_i}, E_i)$ in the cell Ω_i:

$$(5.1\text{i}) \qquad m_i \frac{d}{dt}\tau_i - \sum_{r=1}^{R(i)} L_{r,r+1} \boldsymbol{V^\star_{r,r+1}} \cdot \boldsymbol{N_{r,r+1}} = 0,$$

$$(5.1\text{ii}) \qquad m_i \frac{d}{dt}\boldsymbol{V_i} + \sum_{r=1}^{R(i)} L_{r,r+1} P^\star_{r,r+1} \boldsymbol{N_{r,r+1}} = \boldsymbol{0},$$

$$(5.1\text{iii}) \qquad m_i \frac{d}{dt}E_i + \sum_{r=1}^{R(i)} L_{r,r+1} \left(P\boldsymbol{V}\right)^\star_{r,r+1} \cdot \boldsymbol{N_{r,r+1}} = 0,$$

where the face fluxes $\boldsymbol{V^\star_{r,r+1}}$, $P^\star_{r,r+1}$ are evaluated by our solver. For the time discretization of (5.1) we use a classical forward Euler scheme. A more sophisticated time discretization is not required here, since the scheme is only first order accurate in space. However, time discretization of (5.1) should be done carefully so that all the properties of the semidiscrete system are kept. They are as follows:

- the variation of volume is coherent with the vertex motion;
- momentum and total energy are conserved;
- the scheme satisfies an entropy inequality.

The first two properties would impose an explicit time discretization; the third would impose an implicit discretization. We choose an explicit time discretization, knowing that the entropy inequality will be a priori satisfied under a CFL-type condition.

We assume to know the physical properties in the cell Ω_i and the geometrical characteristics of the cell at the beginning of the time step t_n, i.e., τ_i^n, $\boldsymbol{V_i^n}$, E_i^n, P_i^n, X_r^n, and Y_r^n. We are going to compute their values at t^{n+1} and we set $\Delta t = t^{n+1} - t^n$.

5.1. Mesh motion and variation of volume. The nodal solver provides the vertex velocities $\boldsymbol{V_r^\star}$ and the face pressures at $P^{\star,i}_{r,r+\frac{1}{2}}$, $P^{\star,i}_{r+\frac{1}{2},r+1}$ from the physical variables and geometry characteristics evaluated at time t^n. The explicit time integration of the trajectory equation provides the location of vertices for any time $t \in [t^n, t^{n+1}]$:

$$(5.2) \qquad \begin{aligned} X_r(t) &= X_r^n + (t - t^n)u_r^\star, \\ Y_r(t) &= Y_r^n + (t - t^n)v_r^\star. \end{aligned}$$

In this way, one gets the location of the vertices at time t^{n+1}:

$$(5.3) \qquad \begin{aligned} X_r^{n+1} &= X_r^n + u_r^\star \Delta t, \\ Y_r^{n+1} &= Y_r^n + v_r^\star \Delta t. \end{aligned}$$

From this we deduce that $(L_{r,r+1}\boldsymbol{N_{r,r+1}})(t) = [Y_{r+1}(t) - Y_r(t), -(X_{r+1}(t) - X_r(t))]^t$ is linear in time, so that

$$(5.4) \qquad \int_{t^n}^{t^{n+1}} (L_{r,r+1}\boldsymbol{N_{r,r+1}})(t)\mathrm{d}t = \frac{\Delta t}{2}\left[(L_{r,r+1}\boldsymbol{N_{r,r+1}})^n + (L_{r,r+1}\boldsymbol{N_{r,r+1}})^{n+1}\right].$$

This last result enables us to write an approximation of the volume equation which is coherent with the mesh motion, namely,

(5.5)
$$m_i \left(\tau_i^{n+1} - \tau_i^n \right) - \frac{\Delta t}{4} \sum_{r=1}^{R(i)} \left[(L_{r,r+1} \boldsymbol{N_{r,r+1}})^n + (L_{r,r+1} \boldsymbol{N_{r,r+1}})^{n+1} \right] \cdot \left(\boldsymbol{V_r^\star} + \boldsymbol{V_{r+1}^\star} \right) = 0.$$

Remark 5. We recall that (5.1i) is completely equivalent to the evolution equation of $\mathcal{A}_i$ (area of cell Ω_i), since $m_i \tau_i = \mathcal{A}_i$ and m_i is constant over time; see section 3.2. Knowing that the nodal velocity is computed at time t^n, the right-hand side of (5.1i) is a linear function of time over $[t^n, t^{n+1}]$ thanks to (5.2). Hence, the time integration formula given by (5.4) is exact. Consequently, we can write $\tau_i^{n+1} = \frac{\mathcal{A}_i^{n+1}}{m_i}$. In a nutshell, the second order time integration of the volume flux provides a rigorous compatibility between the specific volume equation and the mesh motion.

5.2. Momentum and total energy. The approximation of the momentum and the total energy equation is fully explicit in order to conserve exactly the momentum and the total energy. The lengths (of edges) and the normals have the same definition as previously. We get

(5.6) $$m_i \left(\boldsymbol{V_i^{n+1}} - \boldsymbol{V_i^n} \right) + \frac{\Delta t}{2} \sum_{r=1}^{R(i)} L_{r,r+1}^n \left(P_{r,r+\frac{1}{2}}^{\star,i} + P_{r+\frac{1}{2},r+1}^{\star,i} \right) \boldsymbol{N_{r,r+1}^n} = \boldsymbol{0},$$

and for the total energy

(5.7) $$m_i \left(E_i^{n+1} - E_i^n \right) + \frac{\Delta t}{2} \sum_{r=1}^{R(i)} L_{r,r+1}^n \left(P_{r,r+\frac{1}{2}}^{\star,i} \boldsymbol{V_r^\star} + P_{r+\frac{1}{2},r+1}^{\star,i} \boldsymbol{V_{r+1}^\star} \right) \cdot \boldsymbol{N_{r,r+1}^n} = 0.$$

5.3. Time step limitation. The time step is evaluated following two criteria. The first is a standard CFL criterion which guarantees heuristically the monotone behavior of the entropy. The second is more intuitive, but appears very useful in practice: we limit the variation of the volume of cells over one time step.

5.3.1. CFL criterion. We propose a CFL-like criterion in order to ensure a positive entropy production in cell Ω_i during the time step. At time t_n, for each cell Ω_i we denote by λ_i^n the minimal value of the distance between two nodes of the cell. We define

$$\Delta t_E = C_E \min_{i=1,\dots,I} \frac{\lambda_i^n}{c_i^n},$$

where C_E is a strictly positive coefficient and c_i is the sound speed in the cell. The coefficient C_E is computed heuristically, and we provide no rigorous analysis which allows such formula. However, extensive numerical experiments show that $C_E = 0.3$ is a value which provides good numerical results. We have also checked that this value is compatible with a monotone behavior of entropy. The rigorous derivation of this criterion could be obtained by computing the time step which ensures a positive entropy production in cell Ω_i from time t^n to t^{n+1}.

5.3.2. Criterion on the variation of volume. Using (5.2), we can compute the area of the cell i at any time $t \in [t^n, t^{n+1}]$. Indeed, we have

(5.8)
$$\mathcal{A}_i(t) = \frac{1}{2} \sum_{r=1}^{R(i)} [X_r^n + (t - t^n)u_r^\star] [Y_{r+1}^n + (t - t^n)v_{r+1}^\star]$$
$$- [Y_r^n + (t - t^n)v_r^\star] [X_{r+1}^n + (t - t^n)u_{r+1}^\star].$$

Simple algebra gives

$$\frac{d}{dt}\mathcal{A}_i(t^n) = \frac{1}{2} \sum_{r=1}^{R(i)} \left(u_r^\star Y_{r+1}^n + v_{r+1}^\star X_r^n - u_{r+1}^\star Y_r^n - v_r^\star X_{r+1}^n \right).$$

After a Taylor expansion we estimate the area at $t = t^{n+1}$ by

$$\mathcal{A}_i^{n+1} = \mathcal{A}_i^n + \frac{d}{dt}\mathcal{A}_i(t^n)\Delta t.$$

Let C_V be a strictly positive coefficient, $C_V \in]0, 1[$. We look for Δt such that

$$\frac{|\mathcal{A}_i^{n+1} - \mathcal{A}_i^n|}{\mathcal{A}_i^n} \le C_V.$$

To do so, we define

$$\Delta t_V = C_V \min_{i=1,\dots,I} \left\{ \frac{\mathcal{A}_i^n}{\left| \frac{d}{dt}\mathcal{A}_i(t^n) \right|} \right\}.$$

For numerical applications, we choose $C_V = 0.1$.

Finally, the estimation of the next time step Δt^{n+1} is given by

(5.9)
$$\Delta t^{n+1} = \min \left(\Delta t_E, \Delta t_V, C_M \Delta t^n \right),$$

where Δt^n is the current time step and C_M is a multiplicative coefficient, which allows the time step to increase. We generally set $C_M = 1.01$.

5.4. Description of the algorithm.
1. **Initialization**
   At time $t = t^n$ we know in each cell Ω_i, $i = 1, \dots, I$, the fluid variables τ_i^n, $\boldsymbol{V_i^n}$, E_i^n, ρ_i^n, c_i^n, P_i^n and the geometrical characteristics $X_r^n, Y_r^n, L_{r,r+1}^n$, $\boldsymbol{N_{r,r+1}^n}$ for $r = 1, \dots, R(i)$.
2. **Nodal solver**
   - For each internal vertex M_q, $q = 1, \dots, Q$, we first compute the velocity $\boldsymbol{V_q^\star}$ by solving the linear system (4.15). Then we evaluate the edge pressures $P_{q,k}^{\star,k}$ and $P_{q,k}^{\star,k-1}$ with (4.12) for each edge impinging on M_q.
   - For each boundary vertex, we first compute the velocity $\boldsymbol{V_q^\star}$ by solving (4.21) or (4.24). Then we calculate the edge pressures $P_{q,k}^{\star,k}$ and $P_{q,k}^{\star,k-1}$ using (4.20).
3. **Time step limitations**
   We compute Δt_V and Δt_E; then we predict Δt^{n+1} from $\Delta t^{n+1} = \min(\Delta t_E, \Delta t_V, C_M \Delta t^n)$.

4. **Update of the geometrical quantities**
   We compute X_r^{n+1} and Y_r^{n+1} from (5.3); then we deduce $L_{r,r+1}^{n+1}$ and $\boldsymbol{N_{r,r+1}^{n+1}}$.

5. **Update of the physical variables**
   We compute the face fluxes from the vertex velocity and the edge pressures; then we get τ_i^{n+1}, $\boldsymbol{V_i^{n+1}}$, and E_i^{n+1} from (5.5), (5.6), and (5.7).

6. **Equation of state**
   The internal energy is given by $\varepsilon_i^{n+1} = E_i^{n+1} - \frac{1}{2}\|\boldsymbol{V_i^{n+1}}\|^2$; then we get the pressure P_i^{n+1} and the isentropic sound speed c_i from the equation of state.

6. Numerical results. In this section, we present several test cases in order to validate our numerical scheme. For each case we use a perfect gas equation of state, namely $P = (\gamma - 1)\rho\varepsilon$, where γ is the adiabatic index. We begin by several classical one-dimensional test cases characterized by the presence of shock waves, of various strengths, rarefaction waves, and contact discontinuities. We also provide an isentropic compression. For all these test cases an analytical solution is available so that we can make accurate comparisons. Then, we give an original test representative of the domain of hydrodynamic instabilities. The aim of this test is to show the ability of our scheme to reproduce the growth of such instabilities in the linear regime. Last, we propose a two-dimensional test case which consists in imploding a double layer cylindrical shell under an anisotropic pressure load.

6.1. Multimaterial Sod's shock tube problem. We are concerned with a multimaterial variant of Sod's shock tube problem defined in [26]. We consider a shock tube of unity length (see Figure 6.1). At the initial time, the states on the left- and right-hand sides of $x = 0.5$ are constant. The left-hand state is a high pressure fluid characterized by $(\rho_l, P_l, u_l) = (1, 1, 0)$, and the right-hand state is a low pressure fluid defined by $(\rho_r, P_r, u_r) = (0.125, 0.1, 0)$. The equation of state is defined on the left by $\gamma_l = \frac{7}{5}$ and by $\gamma_r = \frac{5}{3}$ on the right. The computational domain is defined by $(x, y) \in [0,1] \times [0, 0.1]$. The initial mesh is a Cartesian grid, and we denote by n_x and n_y the number of cells in the x and y directions. The boundary conditions are wall boundary conditions: the normal velocity is set to zero. Three simulations are done with $n_y = 10$ and $n_x = 100$, $n_x = 200$, and finally $n_x = 400$ in order to check the mesh convergence of the scheme. The time step is evaluated following (5.9). In Figure 6.2, we compare the profiles of the physical quantities at $t = 0.2$ with the analytical quantities for three different meshes. The profiles are similar to what could be obtained with a one-dimensional first order Lagrangian scheme based on the acoustic solver; see the interpretation of our scheme in section 4.6.1. The shock is smeared on several cells, and the fan is correctly described for a first order scheme. The contact discontinuity is resolved in several cells; this is a consequence of the entropic nature of the solver. We notice an undershoot for the density profile and an overshoot for the internal energy profile which are classical for Lagrangian methods. As expected, the finer the mesh is, the better the results are.
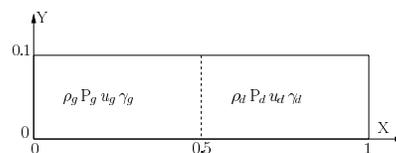

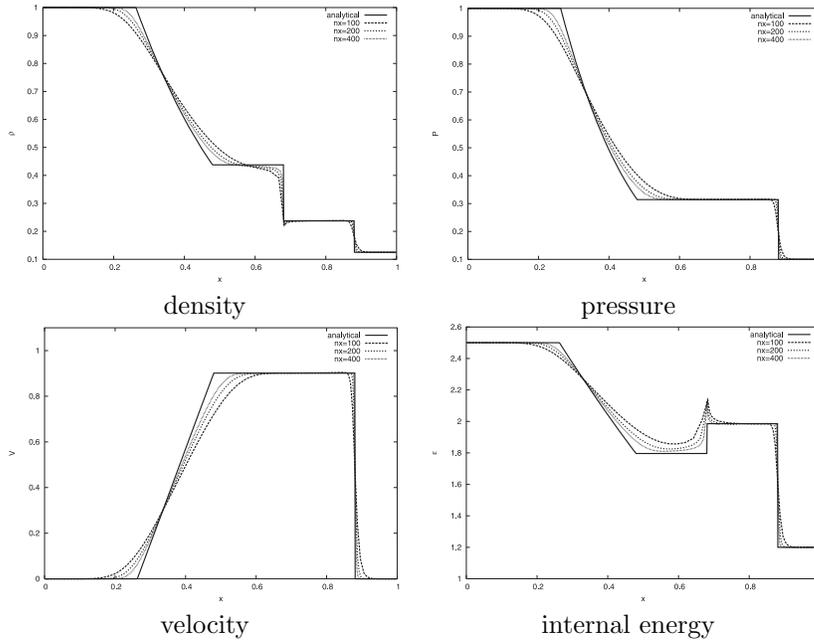FIG. 6.1. *Initial data for Sod's shock tube test case.*

density

pressure

velocity

internal energy

FIG. 6.2. *Cross-section at $t = 0.2$, comparison with the analytical solution.*

6.2. Noh's test case. Noh's test case is the implosion of a cylinder of unit radius. The cylinder is filled with a monoatomic perfect gas ($\gamma = 5/3$). The initial state is $(\rho^0, P^0, \boldsymbol{V^0}) = (1, 0, -\boldsymbol{e_R})$, where $\boldsymbol{e}_R$ represents the radial unit vector. This case, defined by Noh in [23], admits a self-similar solution: a shock wave moves inwards at the constant speed $D = 1/3$. The symmetry of the problem enables us to limit the computational domain to an angular sector of angle Θ; see Figure 6.3. The mesh consists of regular angular sectors, and the domain is meshed with triangles near the center and with quadrangles elsewhere. This enables us to respect the radial symmetry of the solution. We denote by n_x (resp., n_y) the number of layers (resp., angular sectors). In what follows, $\theta = \frac{\Theta}{n_y}$. The test case is initialized with $P^0 = 10^{-6}$. The boundary conditions are wall conditions on the two external edges (hence zero normal velocity), and we impose a constant pressure $P^\star = P^0$ on the external radius $R = 1$. The time step is computed following the condition (5.9). In Figure 6.4 we have represented the results at time $t = 0.6$ for three meshes defined with $\Theta = 12°$ and $(n_x, \theta) = (100, 4°)$, $(200, 2°)$, and $(400, 1°)$. The convergence behavior of the scheme is very satisfactory. The timing, the density levels, and the pressure levels after the shock wave are correct. As for Sod's problem, we notice an overshoot for the internal energy and an undershoot for the density that are characteristic of the wall heating phenomena; see [23]. Figure 6.5 displays the mesh at $t = 0.6$ for $\Theta = 90°$ and $(n_x, \theta) = (100, 2°)$, and one can see that the cylindrical symmetry is perfectly respected.

6.3. Kidder's isentropic compression. In [17], Kidder has analytically computed the solution of the isentropic compression of a cylindrical shell filled with perfect gas. We briefly recall the main features of this solution in order to define the test case. Initially, the shell has the internal (resp., external) radius r_1 (resp., r_2). Let P_1, P_2,
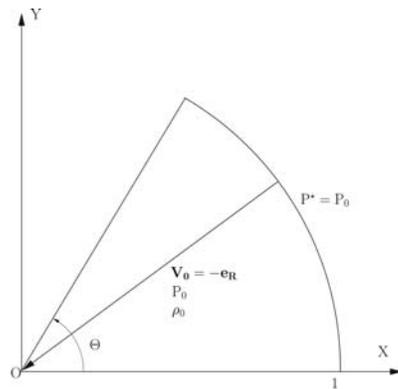
FIG. 6.3. *Noh's case: initial conditions.*

density

pressure

velocity

internal energy
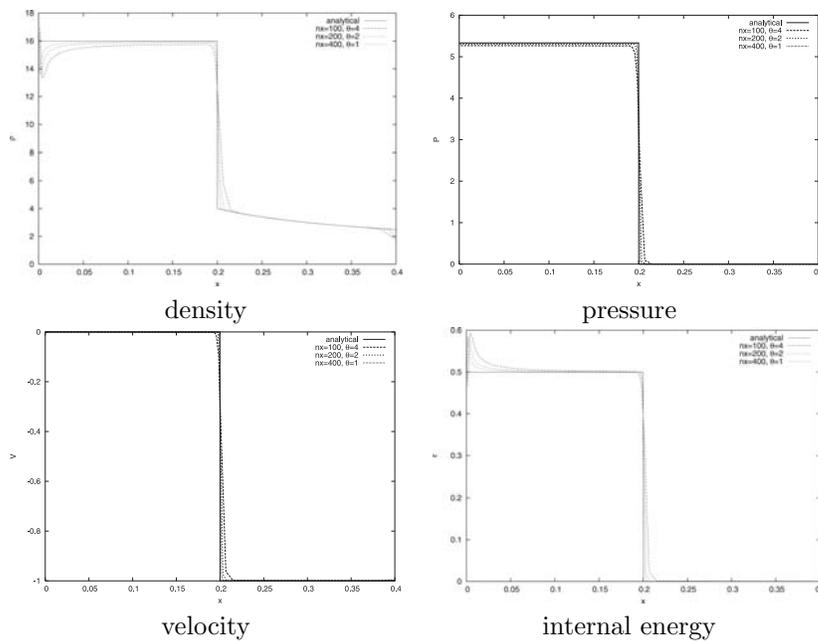
FIG. 6.4. *Cross-section for Noh's case at $t = 0.6$, comparison with the analytical solution.*

ρ_1, and ρ_2 be the pressures and densities located at r_1 and r_2. Since the compression is isentropic, we define $s = \frac{P_2}{\rho_2^\gamma}$ and we have $\rho_1 = \rho_2 (\frac{P_1}{P_2})^{\frac{1}{\gamma}}$. The initial density and pressure profiles are given by (for $r \in [r_1, r_2]$)

$$\rho^0(r) = \left(\frac{r_2^2 - r^2}{r_2^2 - r_1^2} \rho_1^{\gamma-1} + \frac{r^2 - r_1^2}{r_2^2 - r_1^2} \rho_2^{\gamma-1} \right)^{\frac{1}{\gamma-1}},$$

$$P^0(r) = s \left(\rho^0(r) \right)^\gamma.$$

The initial velocity is set to zero: $u_0(r) = 0$. The value of γ is set to $\gamma = 1 + \frac{2}{\nu}$ with $\nu = 1, 2, 3$ whether we have a planar, cylindrical, or spherical symmetry. These values are used in order to obtain a fully analytical solution. In our case we have $\nu = 2$, and

Mesh   Zoom near the origin
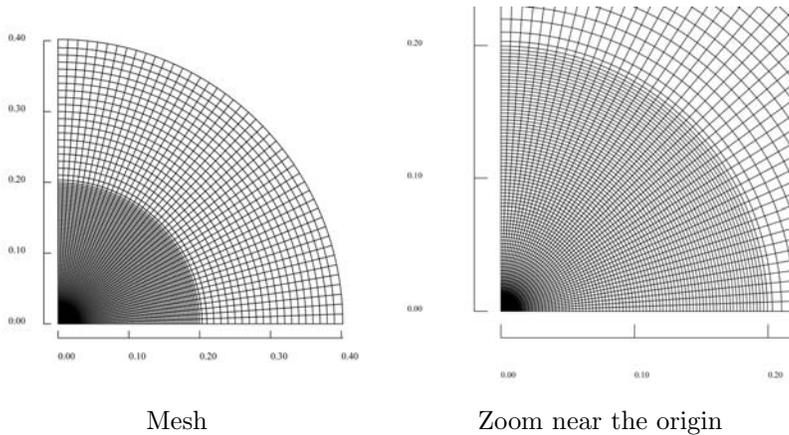
FIG. 6.5. *Noh's case: mesh at $t = 0.6$.*

therefore $\gamma = 2$. The focusing time τ of the shell is defined (for these parameters) by

$$\tau = \sqrt{\frac{\gamma - 1}{2} \frac{r_2^2 - r_1^2}{c_2^2 - c_1^2}},$$

where $c_i = \sqrt{s\gamma\rho_i^{\gamma-1}}$ for $i = 1, 2$ is the isentropic sound speed at $r = r_i$. The isentropic compression is obtained by imposing the following pressure laws at the internal and external faces of the shell:

$$P(R(r_1, t), t) = P_1 h(t)^{-\frac{2\gamma}{\gamma-1}},$$
$$P(R(r_2, t), t) = P_2 h(t)^{-\frac{2\gamma}{\gamma-1}}.$$

Let $R(r, t)$ be the Eulerian radius (i.e., $R = \sqrt{X^2 + Y^2}$) at $t > 0$ of a fluid particle initially located on the circle of radius r. Looking for a solution of the form $R(r, t) = h(t)r$, we get

$$h(t) = \sqrt{1 - \left(\frac{t}{\tau}\right)^2}.$$

The analytical forms of the physical variables at $t \in [0, \tau[$ are

$$\rho(R(r, t), t) = h(t)^{-\frac{2}{\gamma-1}} \rho^0 \left[\frac{R(r, t)}{h(t)}\right],$$
$$u(R(r, t), t) = \frac{d}{dt} h(t) \frac{R(r, t)}{h(t)},$$
$$P(R(r, t), t) = h(t)^{-\frac{2\gamma}{\gamma-1}} P^0 \left[\frac{R(r, t)}{h(t)}\right].$$

In this test case, we have used the parameters $r_1 = 0.9$, $r_2 = 1$, $P_1 = 0.1$, $P_2 = 10$, and $\rho_2 = 10^{-2}$. From this, we get $\rho_1 = 10^{-3}$, $s = 10^5$, and $\tau = 7.265 \ 10^{-3}$. The computational domain consists of the quarter of an annulus; see Figure 6.6. Once
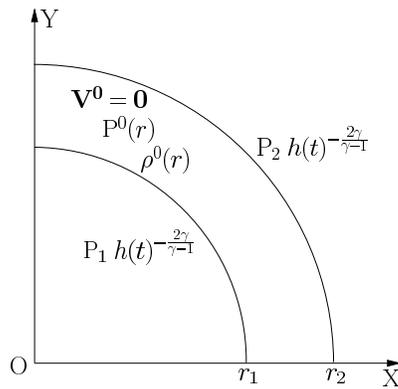
FIG. 6.6. *Initial conditions for Kidder's isentropic compression.*

Time evolution of the external radius   Time evolution of the average density

Density at $t = 0.99\,\tau$ Entropy parameter at $t = 0.99\,\tau$
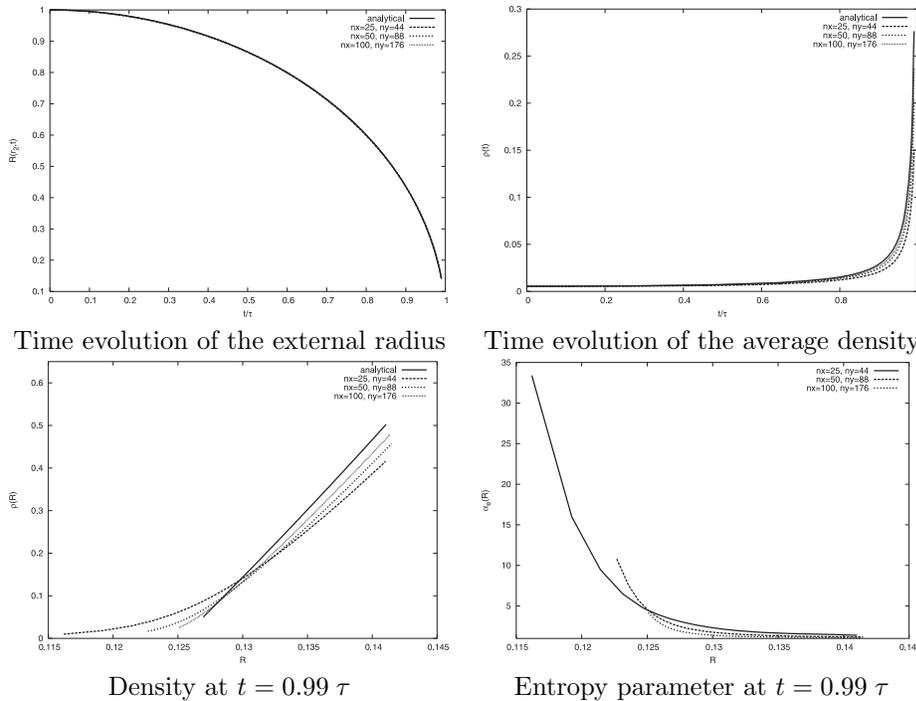
FIG. 6.7. *Kidder's isentropic compression, comparison with the analytical solution.*

more, we impose wall boundary conditions on the axes $X = 0$, $Y = 0$ and the previous pressure laws on the internal and external faces of the domain. The simulations are run on regular polar meshes defined by $(n_x, n_y) = (25, 44)$, $(50, 88)$, $(100, 176)$. The computations are run up to a final time which is very close to the focusing time, i.e., $t = 0.99\,\tau$. In all that follows, the time is adimensionalized by the focusing time τ.

Figure 6.7, where the variation of the external radius of the shell is plotted, shows the excellent agreement with the analytical solution. The agreement is good for the average density[2] $\bar{\rho}(t)$ near the focusing point; however, the numerical values

---

[2] $\bar{\rho}(t)$ is evaluated from the analytical formula $\bar{\rho}(t) = 0.5(\rho_1 + \rho_2)h(t)^{-2}$.

are smaller than the exact ones. There exists a gap between numerical and analytical density profiles at the final time. This gap gets smaller and smaller with mesh refinement; thus we believe it is a consequence of the numerical diffusion. This observation is confirmed by the profile of the entropy parameter $\alpha_e = \frac{P}{s\rho^\gamma}$. It indicates the entropy production of the scheme, and we have $\alpha_e = 1$ in the analytical case. The gap between the exact solution and the numerical one is large on the internal face of the shell when the mesh is coarse, and it also gets smaller with mesh refinement. The large entropy production of the scheme degrades the simulated compression, which explains the shape of the density profile on the internal face of the shell.

6.4. Saltzman's shock tube. We consider now the movement of a planar shock wave on a Cartesian grid that has been stretched [10]. This is a well-known difficult test case that enables us to validate the robustness of our scheme when the mesh is not aligned with the fluid flow. The computational domain is the rectangle $(x, y) \in [0, 1] \times [0, 0.1]$. The initial mesh is obtained by transforming a uniform grid of 100×10 cells with the mapping

$$x_{str} = x + (0.1 - y)\sin(x\pi),$$
$$y_{str} = y.$$

For the material we use the equation of state of a monoatomic gas ($\gamma = 5/3$). The initial state is $(\rho^0, P^0, \boldsymbol{V^0}) = (1, 0, 0)$. The boundary condition at $x = 0$ is a normal velocity $V^\star = -1$ (inflow velocity). On all the other boundaries, we set up wall conditions.

The exact solution is a planar shock wave that moves at speed $D = 4/3$ from left to right. The propagation of the shock wave at $t = 0.6$ is displayed in Figure 6.8. The important result is that our scheme preserves the one-dimensional solution very well (except for the first and last layers in the vertical direction, this is an effect of up and down wall boundary conditions). Figure 6.9 shows the mesh at $t = 0.75$ when the shock wave hits the right boundary ($x = 1$). Behind the shock wave, the initial mesh is distorted, and all the horizontal lines stay almost parallel with respect to the others. The density profile at $t = 0.6$ is displayed in Figure 6.10. The shock level is not uniform, but it oscillates around the exact value $\rho = 4$.

The robustness of our scheme is clearly demonstrated by this test case: we are able to reach time $t = 0.93$ which corresponds to two successive rebounds of the shock wave on the vertical boundaries of the domain; see Figure 6.11. After this time, the computation stops because the time step becomes too small (less than 10^{-15}). This too small time step occurs when nodes are too close to each other (see Figure 6.11, top left corner). In order to go beyond this time we have to improve the quality of the mesh by using a rezoning procedure and a remapping phase. This is the arbitrary Lagrangian–Eulerian (ALE) extension of our scheme which is under development; it will be the subject of a forthcoming paper.

6.5. Sedov's test case. We consider the propagation of a high intensity cylindrical shock wave generated by a strong explosion; see, for instance, [30]. All the boundary conditions are wall conditions. The gas of interest is monoatomic ($\gamma = \frac{5}{3}$). It is initially at rest ($(\rho^0, P^0, \boldsymbol{V^0}) = (1, 0, 0)$) and we set up an energy spike at the center. The simulation is done first on a Cartesian grid and then on a polar grid. In order to compare the results, the same amount of energy is added for each computation.

On the Cartesian grids, the computational domain is $(x, y) \in [0, 1] \times [0, 1]$. In the case of the coarsest mesh (i.e., $(n_x, n_y) = (50, 50)$), the internal specific energy of
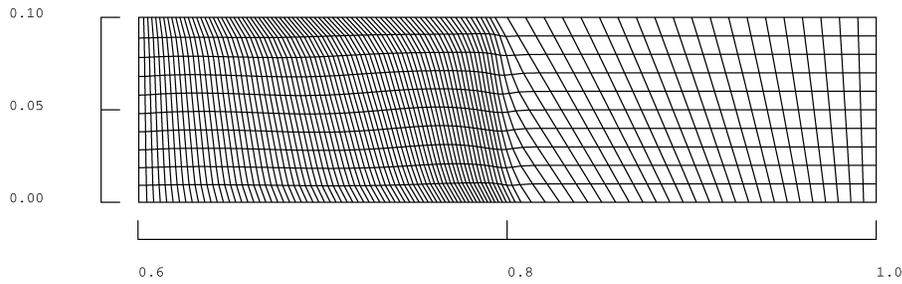
FIG. 6.8. *Saltzman's test: mesh at t = 0.6.*
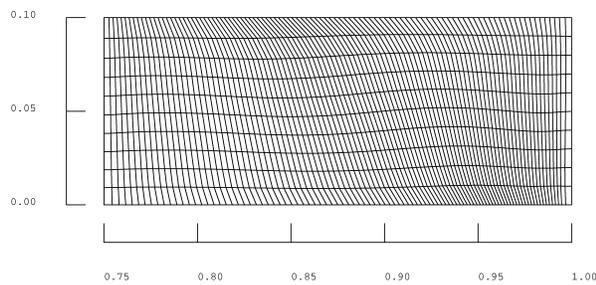
FIG. 6.9. *Saltzman's test: mesh at t = 0.75.*
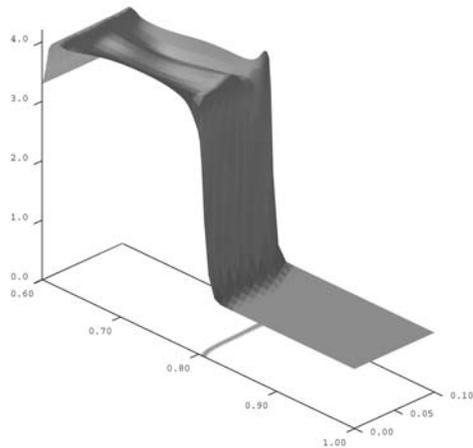
FIG. 6.10. *Saltzman's test: density profile at t = 0.6.*

the first cell is set to $\epsilon^0 = 5000$. This corresponds to subdomain $(x, y) \in [0, 1/50] \times [0, 1/50]$. The finer meshes are $(n_x, n_y) = (100, 100)$ and $(n_x, n_y) = (200, 200)$. In order to have the same amount of energy, we also initialize with the specific internal energy $\epsilon^0 = 5000$ in $[0, 1/50] \times [0, 1/50]$.

In the case of the polar grids, the domain is defined by $(r, \theta) \in [0, 1] \times [0, 90°]$. The
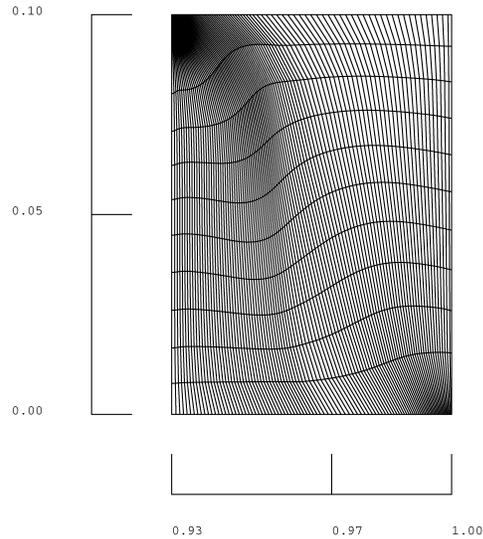
FIG. 6.11. *Saltzman's test: mesh at $t = 0.93$.*

mesh is made of quadrangles with triangles at the center. The parameters (n_x, n_y) correspond to the number of layers in the radial direction and of angular sectors. The coarsest mesh is defined by $(n_x, n_y) = (50, 25)$. We initialize the specific internal energy on triangles and define the subdomain $(r, \theta) \in [0, 1/50] \times [0, 90°]$. As the area to initialize is different in this case, we need to modify the internal energy so that the energy amount is the same as in the case of the Cartesian grid. Thus we choose $\epsilon^0 = 5000\frac{4}{\pi}$. As for the Cartesian mesh, the finest polar grids are $(n_x, n_y) = (100, 50)$ and $(n_x, n_y) = (200, 100)$, and in both cases, the cells to initialize are those in the subdomain $(r, \theta) \in [0, 1/50] \times [0, 90°]$.

Figure 6.12 represents the final mesh at $t = 0.1$ obtained for the two types of meshes. Clearly, our initialization leads to the same results. However, we notice that on the Cartesian grid nonconvex cells appear, but this does not pose any problem to the nodal solver.

The comparison of the density profiles for the two types of grids is done in Figures 6.13, 6.15, and 6.16. We notice that for the polar grid, the cylindrical symmetry of the flow is perfectly preserved; see Figures 6.12 and 6.13. The symmetry is also well preserved on Cartesian grids, as shown in Figure 6.14 on the left, where the density profiles on the diagonal are slightly different from those on the x- and y- axes (which are identical). In Figure 6.14 on the right are represented the density in all cells as function of the centroid radius of each cell. We also observe that the symmetry is well preserved. Consequently, these results on Cartesian grids show the ability of our new scheme to provide good results even when the mesh is not aligned with the flow. Moreover, Figures 6.15 and 6.16 demonstrate that a mesh convergence study for both grids leads to similar results.

6.6. Perturbation of the isentropic Kidder's compression. In this section, we give an original test case representative of the field of hydrodynamic instabilities.
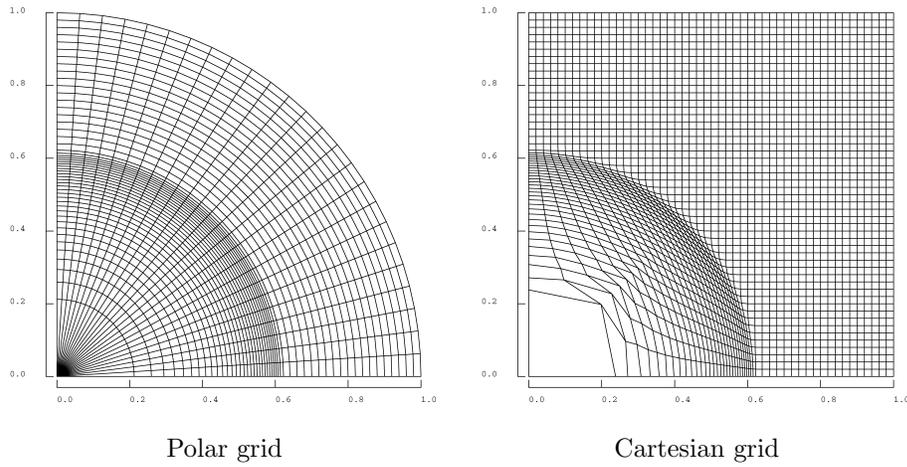
Polar grid   Cartesian grid

FIG. 6.12. *Sedov's test case: mesh at $t = 0.1$ for the polar and Cartesian meshes.*
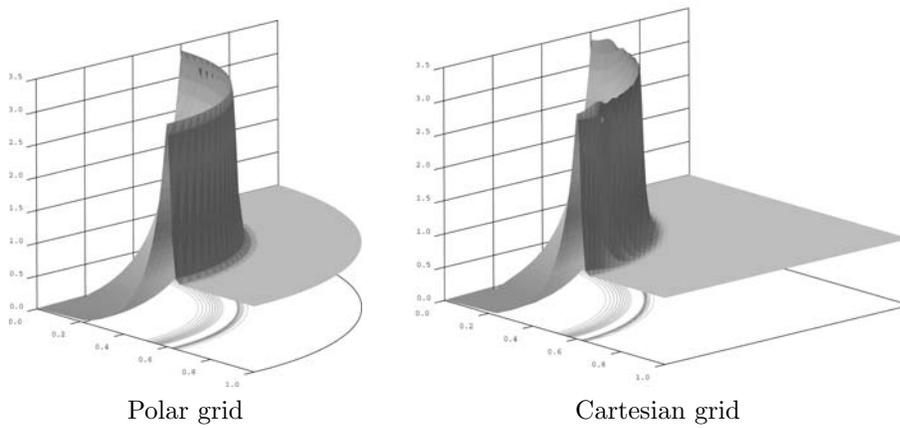

Polar grid   Cartesian grid

FIG. 6.13. *Sedov's test case: density level at $t = 0.1$.*

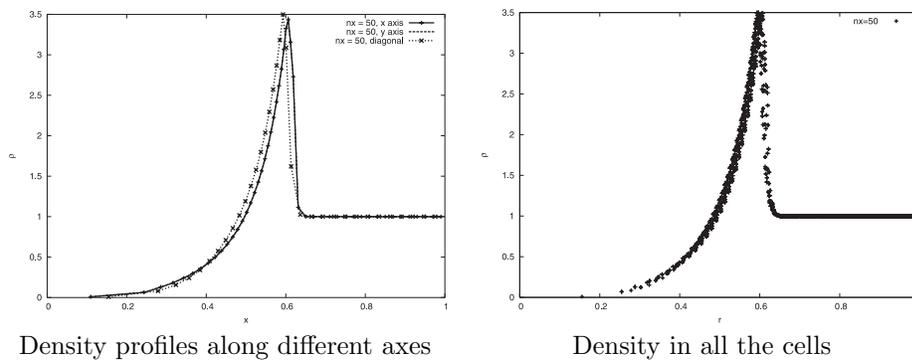Density profiles along different axes   Density in all the cells

FIG. 6.14. *Sedov's test case on Cartesian grid at $t = 0.1$.*
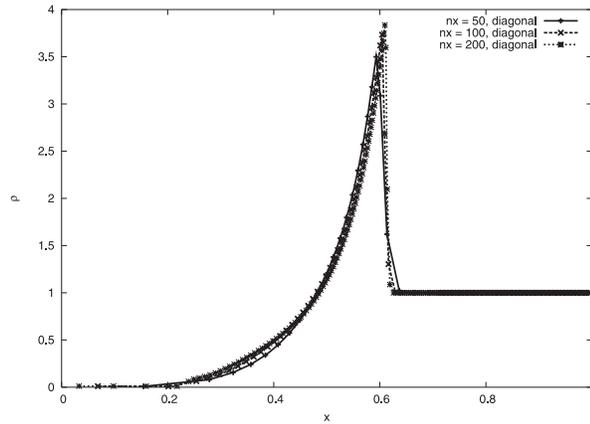
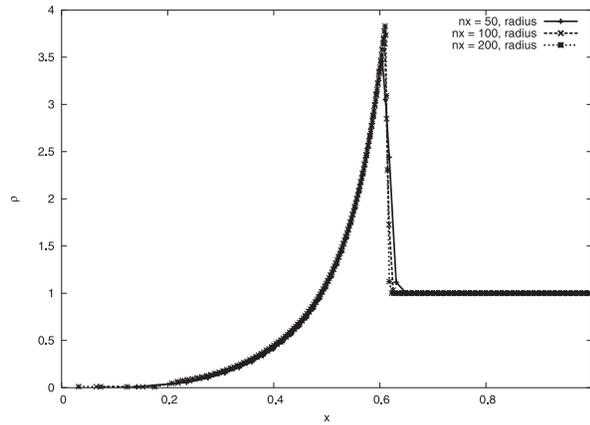FIG. 6.15. *Sedov's test case: Cartesian grid convergence for density profiles at* $t = 0.1$

FIG. 6.16. *Sedov's test case: polar grid convergence for density profiles at* $t = 0.1$.

The aim of this test is to show the ability of our new scheme to reproduce the growth of such instabilities. In order to define the test, we consider the isentropic implosion of a cylindrical shell as in section 6.3. We initially perturb the internal and external faces of the shell; see Figure 6.6. Then, we study the time evolution of the perturbations. An approximate analytical solution is available for the perturbation amplification in the linear regime. This solution is obtained with the technique developed in [13]. We briefly recall the main results about the analytical solution in order to set up the test case. More details can be found in [22] and [3].

First we define the mesh perturbation. We are given a Cartesian frame $(0, x, y)$ and polar coordinates (r, θ). The polar coordinates of the vertices are given by

$$r^p = r + a_0 \xi_r(r, \theta),$$
$$\theta^p = \theta + a_0 \xi_\theta(r, \theta),$$

where a_0 is the amplitude of the initial perturbation. The vector $\boldsymbol{\xi} = \begin{pmatrix} \xi_r \\ \xi_\theta \end{pmatrix}$ is defined by

(6.1)
$$\xi_r(r, \theta) = n \left(A_1 r^{-n-1} + A_2 r^{n-1} \right) \cos(n\theta),$$
$$\xi_\theta(r, \theta) = -n \left(A_1 r^{-n-1} + A_2 r^{n-1} \right) \sin(n\theta).$$
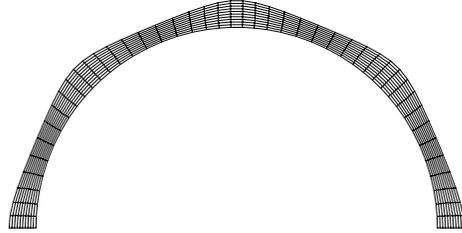
FIG. 6.17. *Perturbed mesh.*

The integer n is the perturbation mode, and A_1, A_2 are constants which are determined by the perturbations ξ_1 and ξ_2 given at the internal and external interfaces, i.e., $\xi_1 = \xi_r(r_1, 0)$ and $\xi_2 = \xi_r(r_2, 0)$. We have

$$
\begin{cases}
A_1 = -\dfrac{1}{n} \dfrac{\xi_1 r_2^{n-1} - \xi_2 r_1^{n-1}}{r_1^{-n-1} r_2^{n-1} - r_1^{n-1} r_2^{-n-1}}, \\[2ex]
A_2 = -\dfrac{1}{n} \dfrac{\xi_1 r_2^{-n-1} - \xi_2 r_1^{-n-1}}{r_1^{-n-1} r_2^{n-1} - r_1^{n-1} r_2^{-n-1}}.
\end{cases}
$$

The analytical form (6.1) is justified by the fact that $\boldsymbol{\xi}$ derives from a potential. We check that $\nabla \cdot \boldsymbol{\xi} = 0$, that is, that the perturbation is incompressible. We have a divergence-free perturbation.

Using the previous results, we get the Cartesian coordinates of the perturbed mesh

(6.2)
$$
\begin{aligned}
x^p &= \left(1 + \frac{a_0}{r}\xi_r\right)\left[x\cos(a_0\xi_\theta) - y\sin(a_0\xi_\theta)\right], \\
y^p &= \left(1 + \frac{a_0}{r}\xi_r\right)\left[x\sin(a_0\xi_\theta) + y\cos(a_0\xi_\theta)\right].
\end{aligned}
$$

This is illustrated by Figure 6.17, which represents the perturbed mesh for the half-annulus of radii $r_1 = 0.9$, $r_2 = 1$, with the following data: perturbation mode $n = 8$, internal and external levels $\xi_1 = 0$, $\xi_2 = 1$, amplitude $a_0 = 0.02$. In [22], we show that the amplification factor $a(\theta, t)$ of the perturbation at the external interface is given by

$$
a(\theta, t) = n\left[A_1 r^{-n-1} G_1(t) + A_2 r^{n-1} G_2(t)\right]\cos(n\theta),
$$

where $t \in [0, 1[$ is the time.[3] The functions G_1 and G_2 are

$$
G_1(t) = \sqrt{1 - t^2}\cos\left[\frac{\sqrt{n}}{2}\log\left(\frac{1-t}{1+t}\right)\right],
$$

$$
G_2(t) = \frac{1}{2}\sqrt{1 - t^2}\left[\left(\frac{1-t}{1+t}\right)^{\sqrt{n}/2} + \left(\frac{1+t}{1-t}\right)^{\sqrt{n}/2}\right].
$$

---

[3] The time is adimensionalized by the focusing time τ.

Next, we present the results for the following cases: modes 4 and 8 with a perturbation of the external interface and mode 8 with a perturbation of the internal and external interfaces. For a given mode, we first define a mesh compatible with this mode, i.e., with enough angular sectors per wave length. Then, we compute the nonperturbed implosion and store the location of the vertex of the external face that corresponds to $\theta = 0$, namely $R(r_2, t)$. Then we perturb the mesh according to (6.2). An implosion simulation is done on this perturbed mesh. Then we store $R_p(r_2, t)$, the location of the same vertex. The amplification factor is defined by the ratio

$$a_{\text{num}}(t) = \frac{R^p(r_2, t) - R(r_2, t)}{a_0}.$$

In each of the perturbed simulations, the initial amplitude is set to $a_0 = 10^{-6}$ in order to stay in the linear phase. The final time of each simulation is $t = 0.99$. The time step follows (5.9).

6.6.1. Mode $n = 4$, $\xi_1 = 0$, $\xi_2 = 1$, $a_0 = 10^{-6}$. The computational domain is defined using the symmetries of mode 4, i.e., $(r, \theta) \in [r_1, r_2] \times [0, \frac{\pi}{2}]$ (see Figure 6.18). We use equiangular meshes defined by $(n_x, n_y) = (25, 44)$, $(n_x, n_y) = (50, 88)$, and $(n_x, n_y) = (100, 176)$.
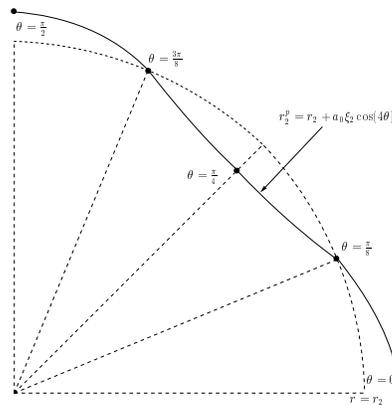
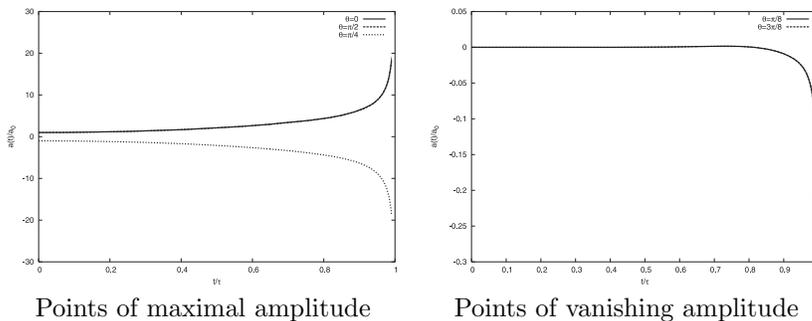FIG. 6.18. *Mode $n = 4$, location of the vertices of interest.*

Points of maximal amplitude   Points of vanishing amplitude

FIG. 6.19. *Mode $n = 4$, time evolution of the external perturbation for several vertices of interest.*

In Figure 6.19, we show the results for the coarsest mesh. The time evolution of the amplitude for the vertices defined by $\theta = 0$, $\pi/8$, $\pi/4$, $3\pi/8$, $\pi/2$ (see Figure 6.18)
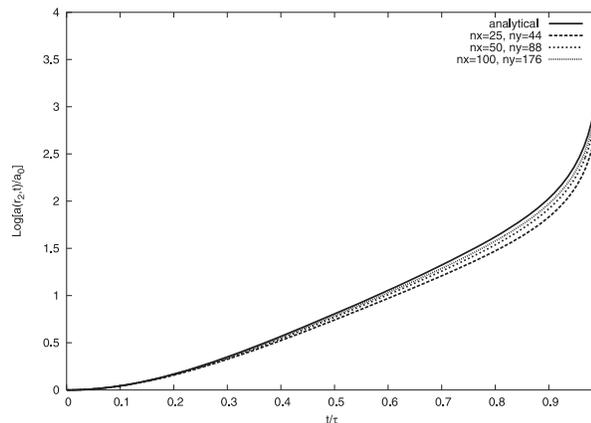
FIG. 6.20. *Mode $n = 4$, time evolution of the amplitude of the external perturbation.*

is stored. We see that the expected symmetries for the vertices $\theta = 0$, $\pi/4$, $\pi/2$ are perfectly respected. Moreover, the amplification factor for the vertices defined by $\theta = \pi/8$, $3\pi/8$ is almost null, but we notice a very small amplification, on the order of 1%, when we are near the focusing. In Figure 6.20, we plot the time evolution of the perturbation obtained numerically for the three meshes and the analytical solution. The comparison is satisfactory since the numerical amplification is coherent with the analytical one. This comparison is even more satisfactory as the scheme is only first order in time and space.

Mesh at $t/\tau = 0.98$ Zoom
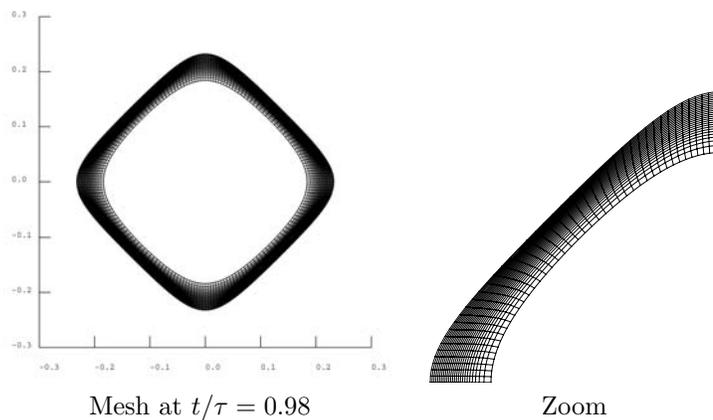
FIG. 6.21. *Mode $n = 4$, nonlinear phase $a_0 = 10^{-3}$.*

We present in Figure 6.21 the mesh that corresponds to a perturbed simulation near the focusing time. The initial mesh is defined by $(n_x, n_y) = (25, 176)$. The initial amplitude is set to $a_0 = 10^{-3}$ so that, at the final time, we are in the nonlinear regime.

6.6.2. Mode $n = 8$, $\xi_1 = 0$, $\xi_2 = 1$, $a_0 = 10^{-6}$. The computational domain is defined using the symmetries of the mode 8, i.e., $(r, \theta) \in [r_1, r_2] \times [0, \frac{\pi}{2}]$. We use equi-angular meshes with $(n_x, n_y) = (25, 44)$, $(n_x, n_y) = (50, 88)$, and $(n_x, n_y) = (100, 176)$. Figure 6.22 shows a good agreement with the analytical solution for the time evolution
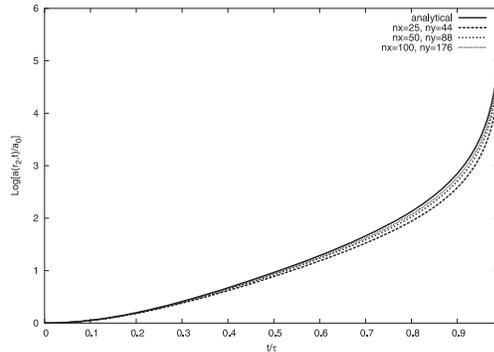
FIG. 6.22. *Mode $n = 8$, time evolution of the amplitude of the external perturbation.*

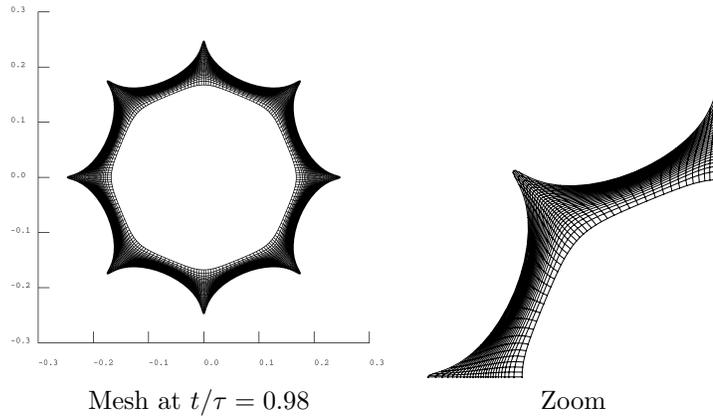of the amplitude of the external perturbation. As for the $n = 4$ mode case, the scheme converges by lower values.

Mesh at $t/\tau = 0.98$ Zoom

FIG. 6.23. *Mode $n = 8$, nonlinear phase for $a_0 = 10^{-3}$.*

In Figure 6.23 we display the mesh obtained during the nonlinear phase for the flow perturbed on the full geometry. The initial mesh is defined by $(n_x, n_y) = (25, 176)$. The initial amplitude of the perturbation is $a_0 = 10^{-3}$.

6.6.3. Mode $n = 8$, $\xi_1 = 2.565293$, $\xi_2 = 1$, $a_0 = 10^{-6}$. In this case, we have introduced a nonzero initial perturbation on the internal interface. The level of ξ_1 is defined so that at the final time $t = 0.99$, the amplitude of the perturbation on the external face comes back to its initial value. This permits the coupling of the perturbations between the two interfaces. This coupling enables us to get a periodic growth of the perturbation on the internal face. In this case, we use the same meshes and the same domain as in the previous case.

The results are very satisfactory; see Figure 6.24. They show the ability of our scheme to reproduce the coupling of perturbations between the internal and external faces.

6.7. ICF-like test case. In this section, we present a simplified test case of a cylindrical ICF target. The target is made of two materials which have the same
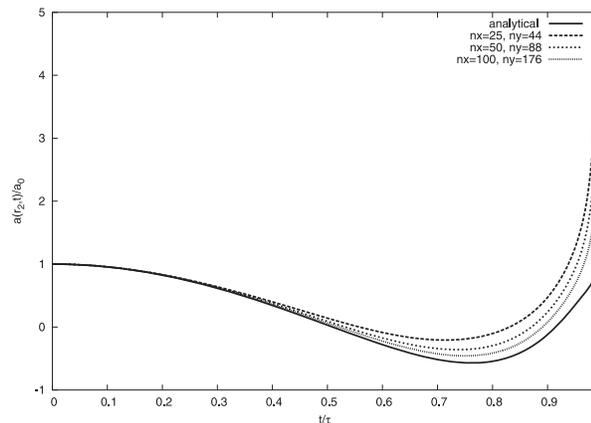
FIG. 6.24. *Coupled mode $n = 8$, growth of the perturbation on the internal interface.*
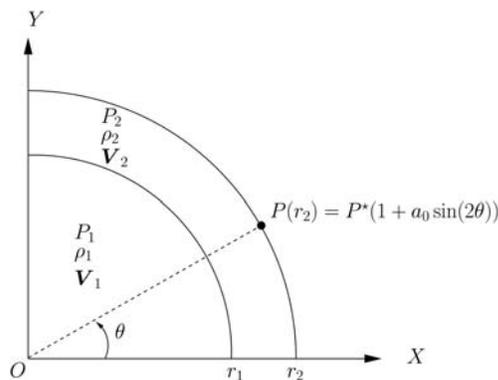

FIG. 6.25. *ICF-like target: initial conditions.*

perfect gas equation of state ($\gamma = 5/3$). The data are chosen to be representative of ICF situations. The interface between the gas and the shell is located at $r_1 = 0.1$, and the external radius of the target is $r_2 = 0.11$; see Figure 6.25. The initial state of the gas is given by $(\rho_1, P_1, \boldsymbol{V_1}) = (0.01, 2.5 \ 10^9, 0)$, and the state inside the shell is $(\rho_2, P_2, \boldsymbol{V_2}) = (1, 2.5 \ 10^{11}, 0)$. On the external surface of the shell, we apply a pressure law $P^\star = 10^{14}(1 + a_0 \sin(2\theta))$. We study this target in two configurations: the first is monodimensional with $a_0 = 0$, and the second is bidimensional with $a_0 = 0.2$. This second configuration may crudely represent the hydrodynamic part of an ICF flow which results from an inhomogeneous irradiation of the target.

For the monodimensional problem the mesh is made of 25 identical angular sectors on $[0, 90°]$ and 200 layers (100 uniform layers in the gas and 100 layers with a geometrical progression in the shell). A geometrical progression is applied so that we have a good representation of the contact discontinuity between the two materials (we have the same mass in the two cells around the interface). The time evolution of internal interface is displayed in Figure 6.26. This shows the two acceleration periods at $t = 1 \ 10^{-9}$ and $t = 3 \ 10^{-9}$ of the interface and at the end the deceleration of the interface until the stagnation time at $t = 5 \ 10^{-9}$. In order to validate our results for the monodimensional configuration, we compare them to the results obtained with a

monodimensional code named CHIVAS. This code uses a von Neumann–Richtmyer-type scheme; see [16]. In Figure 6.26, we compare the trajectory of the internal inter-face with our scheme and with CHIVAS. The two curves can be almost superimposed, which demonstrates the quality of our scheme.

For the bidimensional case we use two types of meshes. One is a polar mesh (see Figure 6.27) with 40 angular sectors on $[0, 90°]$ and 100 layers (50 uniform layers in the gas and 50 layers with a geometrical progression in the shell). The other is a multiblock mesh in which we have a square in the central part of the target and nearly the same mesh as the polar grid for the rest of the domain (see Figure 6.27). Figure 6.28 represents the mesh at $t = 4.4\ 10^{-9}$ for both configurations. The nonuniformity of the pressure on the shell boundary leads to a bidimensional deformation of the internal interface.

Figure 6.29 illustrates one of the advantages of using a multiblock mesh. We can see that the time step in the case of the polar mesh reduces to a very small value $(\approx 1\ 10^{-14})$, whereas for the multiblock mesh we keep a reasonable time step $(\approx 1\ 10^{-13})$. The very small value of the time step for the polar mesh is due to the very small size of the triangular cells located at the center. Moreover, the multiblock mesh makes the computation more robust and enables us to deal with higher nonuniformity values for a_0.
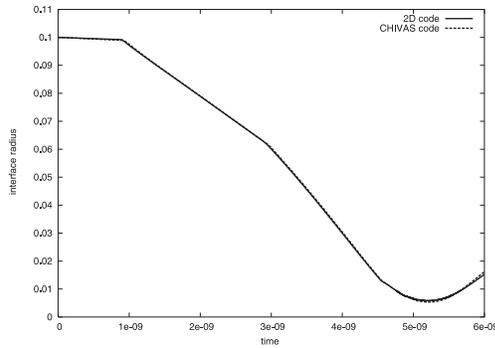

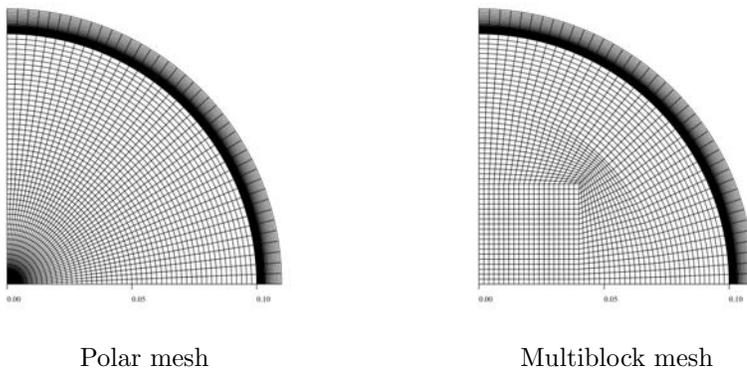FIG. 6.26. *Monodimensional ICF-like test case: time evolution of the internal interface radius.*

Polar mesh   Multiblock mesh

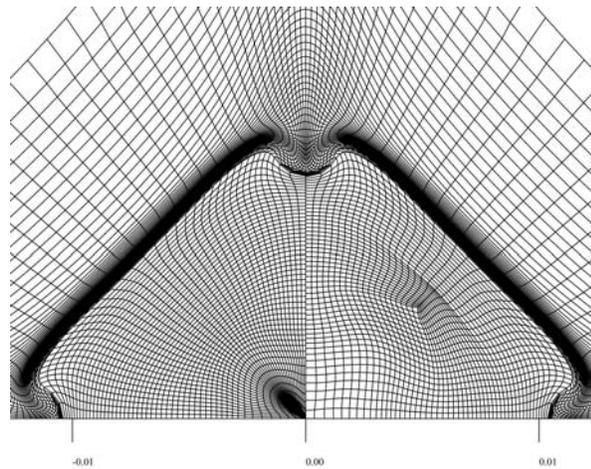FIG. 6.27. *Initial mesh for bidimensional ICF-like test case.*

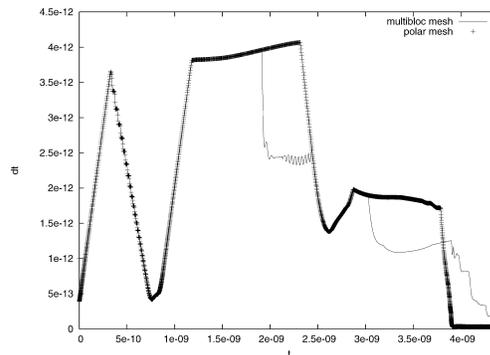FIG. 6.28. *Result for two types of meshes at time* $t = 4.4\ 10^{-9}$.

FIG. 6.29. *Time step during the simulations.*

7. Conclusion and perspectives. We have developed a new Lagrangian cell-centered conservative scheme. This scheme relies on a genuinely two-dimensional nodal solver. It can be interpreted as the two-dimensional generalization of the Godunov acoustic solver. The main new feature of the algorithm is the introduction of four pressures on each edge, two for each node on each side of the edge. This extra degree of freedom allows us to construct a nodal solver that fulfills two properties. First, the conservation of momentum and total energy is ensured. Second, a semidiscrete entropy inequality is provided. The face fluxes and the nodal velocities are all evaluated in a coherent manner. We have checked that, in the case of one-dimensional problems (with planar or cylindrical symmetry), our solver is exactly equivalent to the one-dimensional Godunov acoustic solver.

The scheme is only first order accurate; however it appears to be quite robust and versatile according to the numerical results obtained for the various test cases presented in this paper.

The next step is to develop the axisymmetric extension of our scheme. Then, in order to improve the accuracy of the scheme we will study its second order extension, probably with a MUSCL-type method. This new Lagrangian method looks promising

both as a stand-alone entity but also as a foundation for a more general method which may include ALE and/or adaptive mesh refinement techniques. The uniform cell centering of the solution variables provides a consistent basis for employing a wide range of well-proven remapping and adaptation schemes.

REFERENCES

[1] R. Abgrall, R. Loubère, and J. Ovadia, *A Lagrangian discontinuous Galerkin-type method on unstructured meshes to solve hydrodynamics problems*, Internat. J. Numer. Methods Fluids, 44 (2004), pp. 645–663.

[2] D. J. Benson, *Computational methods in Lagrangian and Eulerian hydrocodes*, Comput. Methods Appl. Mech. Engrg., 99 (1992), pp. 235–394.

[3] J. Breil, L. Hallo, P.-H. Maire, and M. Olazabal-Loumé, *Hydrodynamic instabilities in axisymmetric geometry: Self-similar models and numerical simulations*, Laser Part. Beams, 23 (2005), pp. 155–160.

[4] J. C. Campbell and M. J. Shashkov, *A tensor artificial viscosity using a mimetic finite difference algorithm*, J. Comput. Phys., 172 (2001), pp. 739–765.

[5] E. J. Caramana, M. J. Shashkov, and P. P. Whalen, *Formulations of artificial viscosity for multidimensional shock wave computations*, J. Comput. Phys., 144 (1998), pp. 70–97.

[6] E. J. Caramana, D. E. Burton, M. J. Shashov, and P. P. Whalen, *The construction of compatible hydrodynamics algorithms utilizing conservation of total energy*, J. Comput. Phys., 146 (1998), pp. 227–262.

[7] E. J. Caramana and M. J. Shashkov, *Elimination of artificial grid distortion and hourglass-type motions by means of Lagrangian subzonal masses and pressures*, J. Comput. Phys., 142 (1998), pp. 521–561.

[8] A. Chorin and J. Marsden, *A Mathematical Introduction to Fluid Mechanics*, Springer-Verlag, New York, 1993.

[9] B. Després and C. Mazeran, *Lagrangian gas dynamics in two dimensions and Lagrangian systems*, Arch. Ration. Mech. Anal., 178 (2005), pp. 327–372.

[10] J. K. Dukowicz and B. Meltz, *Vorticity errors in multidimensional Lagrangian codes*, J. Comput. Phys., 99 (1992), pp. 115–134.

[11] J. K. Dukowicz, M. C. Cline, and F. S. Addessio, *A general topology Godunov method*, J. Comput. Phys., 82 (1989), pp. 29–63

[12] S. K. Godunov, A. Zabrodine, M. Ivanov, A. Kraiko, and G. Prokopov, *Résolution numérique des problèmes multidimensionnels de la dynamique des gaz*, Mir, Moscow, 1979.

[13] S. J. Han and B. R. Suydam, *Hydrodynamic instabilities in an imploding cylindrical plasma shell*, Phys. Rev. A, 26 (1982), pp. 926–939.

[14] C. W. Hirt, A. Amsden, and J. L. Cook, *An arbitrary Lagrangian–Eulerian computing method for all flow speeds*, J. Comput. Phys., 14 (1974), pp. 227–253.

[15] W. H. Hui, P. Y. Li, and Z. W. Li, *A unified coordinate system for solving the two-dimensional Euler equations*, J. Comput. Phys., 153 (1999), pp. 596–637.

[16] S. Jacquemot and A. Decoster, *Z scaling of collisional NE-like X-ray lasers using exploding foils. Refraction effects*, Laser Part. Beams, 9 (1991), pp. 517–526.

[17] R. E. Kidder, *Laser-driven compression of hollow shells: Power requirements and stability limitations*, Nuclear Fusion, 1 (1976), pp. 3–14.

[18] L. Landau and E. Lifchitz, *Mécanique des fluides*, Mir, Moscow, 1989.

[19] J. D. Lindl, *Inertial Confinement Fusion*, Springer-Verlag, New York, 1998.

[20] R. Loubère, *Une méthode particulaire Lagrangienne de type Galerkin discontinu. Application à la mécanique des fluides et à l'interaction laser plasma*, Ph.D. thesis, Université Bordeaux 1, Talence, France, 2002.

[21] R. Loubère and M. J. Shashkov, *A subcell remapping method on staggered polygonal grids for arbitrary-Lagrangian-Eulerian methods*, J. Comput. Phys., 209 (2005), pp. 105–138.

[22] P.-H. Maire, J. Breil, L. Hallo, and M. Olazabal-Loumé, *Hydrodynamic instabilities in cylindrical geometry. Self-similar models and numerical simulations*, in Proceedings of the 31st EPS Conference on Plasma Physics, London, 2004.

[23] W. F. Noh, *Errors for calculations of strong shocks using artificial viscosity and an artificial heat flux*, J. Comput. Phys., 72 (1987), pp. 78–120.

[24] R. D. Richtmyer and K. W. Morton, *Difference Methods for Initial-Value Problems*, John Wiley, New York, 1967.

[25] Y. Saillard, *Hydrodynamique de l'implosion d'une cible FCI*, C. R. Acad. Sci. Paris Sér. IV, 1 (2000), pp. 705–718.

[26] G. A. SOD, *A survey of several finite difference methods for systems of nonlinear hyperbolic conservation laws*, J. Comput. Phys., 27 (1978), pp. 1–31.

[27] J. VON NEUMANN AND R. D. RICHTMYER, *A method for the numerical calculations of hydro-dynamical shocks*, J. Appl. Phys., 21 (1950), pp. 232–238.

[28] P. P. WHALEN, *Algebraic limitations on two dimensional hydrodynamics simulations*, J. Comput. Phys., 124 (1996), pp. 46–54.

[29] M. L. WILKINS, *Calculation of elastic-plastic flow*, in Methods in Computational Physics, Vol. 3, Academic Press, New York, 1964, pp. 211–263.

[30] Y. B. ZEL'DOVICH AND Y. P. RAIZER, *Physics of Shock Waves and High-Temperature Hydro-dynamic Phenomena,* Vol. I, Academic Press, New York, 1966.